Two-year observations of the Jupiter polar regions by JIRAM on board Juno

A. Adriani[1], A. Bracco[2], D. Grassi[1], M.L. Moriconi[3], A. Mura[1], G. Orton[4], F. Altieri[1], A. Ingersoll[5], S.K. Atreya[6], J.I. Lunine[7], A. Migliorini[1], R. Noschese[1], A. Cicchetti[1], R. Sordini[1], G. Sindoni[8], C. Plainaki[8], B.M. Dinelli[3], D. Turrini[1], G. Filacchione[1], G. Piccioni[1], F. Tosi[1], and S.J. Bolton[9].

[1]INAF - Istituto di Astrofisica e Planetologia Spaziali, Roma, Italy
[2]Georgia Institute of Technology, Atlanta, Georgia, USA
[3]CNR - Istituto di Scienze dell'Atmosfera e del Clima, Bologna and Roma, Italy
[4]Jet Propulsion Laboratory, California Institute of Technology, Pasadena, California, USA
[5]California Institute of Technology, Pasadena, California, USA
[6]University of Michigan, Ann Arbor, Michigan, USA
[7]Cornell University, Ithaca, New York, USA
[8]Agenzia Spaziale Italiana, Roma, Italy
[9]Southwest Research Institute, San Antonio, Texas, USA

Corresponding author: Alberto Adriani (alberto.adriani@inaf.it)

Key Points:

- The Jupiter's polar cyclonic structures did not change much in two years of observations from February 2017 to February 2019.
- Abundances of some atmospheric minor constituents measured in the hottest spots of the polar regions, higher values registered in the south.
- Earth oceanic cyclones analogies suggest a well-mixed upper boundary layer on Jupiter's Poles.

Abstract

We observed the evolution of Jupiter's polar cyclonic structures over two years between February 2017 and February 2019, using polar observations by the Jovian InfraRed Auroral Mapper, JIRAM, on the Juno mission. Images and spectra were collected by the instrument in the 5-μm wavelength range. The images were used to monitor the development of the cyclonic and anticyclonic structures at latitudes higher than 80° both in the northern and the southern hemispheres. Spectroscopic measurements were then used to monitor the abundances of the minor atmospheric constituents water vapor, ammonia, phosphine and germane in the polar regions, where the atmospheric optical depth is less than 1. Finally, we performed a comparative analysis with oceanic cyclones on Earth in an attempt to explain the spectral characteristics of the cyclonic structures we observe in Jupiter's polar atmosphere.

Plain Language Summary

The Jovian InfraRed Auroral Mapper (JIRAM) is an instrument on-board the Juno NASA spacecraft. It consists of an infrared camera, for mapping both Jupiter's auroras and atmosphere, and a spectrometer.
In February 2017, the complex cyclonic structures that characterize the Jupiter's polar atmospheres were discovered. Here, we report the evolution of those cyclonic structures during the 2 years following the discovery. We use for this purpose infrared maps built by the JIRAM camera images collected at wavelengths around 5 μm.

The cyclones have thick clouds which obstruct most of the view of the deeper atmosphere. However, some areas, near the cyclones, are only covered by thin clouds allowing the spectrometer to see deeper in the atmosphere. In those areas, the instrument was able to detect spectral signatures that permitted estimation of abundances of water vapor, ammonia, phosphine and germane. Those gases are minor but significant constituents of the atmosphere.
Finally, the dynamics of the Jupiter's polar atmosphere are not well understood and are still under study. Here, to suggest possible mechanisms that governs the polar dynamics, we attempted a comparative analysis with some Earth oceanic cyclones that show similarities with the Jupiter ones.

Keywords: Jupiter, Planetary Atmosphere, Polar Regions, Composition, Mesoscale Dynamics

1. Introduction

The Juno mission entered into Jupiter orbit in July, 2016 [Bolton et al. 2017]. The Jovian InfraRed Auroral Mapper, JIRAM, is part of the payload of the spacecraft [Adriani et al. 2017]. Key goals of this instrument are to collect both ~5-μm imaging (M band filter: 4.5 to 5 μm) and spectral observations in the 2-5 μm range with a spectral resolution of about 15 nm to study Jupiter's atmosphere. The methane transparency window, around 5, μm is a spectral region dominated by the atmospheric thermal emission. However, the thermal emission is modulated by the presence of the clouds and, thus, the depth of the infrared sounding depends on the cloud thickness. In the absence of clouds and for small optical thickness the infrared sounding at wavelengths around 5 μm can reach depths of 4-5 bar. The imager focal plane is divided in two areas by the presence of two optical filters: one in band L dedicated to auroral mapping and the other in band M for atmospheric observations. The auroral signal is weaker than the atmospheric thermal emission, and thus the imager has to use different integration times in according with the target of interest. This fact implies that the observations targeting the aurorae or the atmospheric thermal emissions cannot be operated simultaneously. The imager and the spectrometer have a spatial resolution of 250 μrad and are operated simultaneously.
The great advantage of Juno's instruments, compared to all the others that have observed Jupiter for years from Earth and from other space missions, is that Juno is in a polar orbit, allowing an unprecedented view of the planet's poles.

On February 2nd 2017, during the fourth fly-by, JIRAM had the opportunity to observe the polar atmosphere of Jupiter for the first time [Adriani et al. 2018]. Those observations, together with those of the visible JunoCam imager [Hansen et al, 2014], allowed us to survey for the first time the dynamical structure of the polar atmosphere of the planet. The North Pole exhibits a polar cyclone (or NPC) surrounded by eight circumpolar cyclones (or CPCs) while the South Pole is characterized by five cyclones surrounding a polar cyclone. The CPCs have approximately the same size as their respective central polar cyclones; the southern cyclones are larger than the northern ones.

JIRAM's observation of Jupiter's poles has continued since February 2017 during fly-bys with favorable spacecraft attitudes and when auroral observations by JIRAM were not scheduled. For the sake of simplicity we identify **Juno** orbits with the label PJ (PeriJove) followed by the orbit number. The spacecraft attitude was generally not favorable to the JIRAM observations during orbits when the mission optimized the gravitational mapping of Jupiter (GRAV orbits). Additionally, the instrument can only observe targets that are within ±3° **of** the plane orthogonal to the spacecraft spin axis. A limited number of orbits have been dedicated to remote sensing instrumentation on board of Juno. During orbits when the MicroWave Radiometer (MWR) was the prime instrument, JIRAM could observe the planet during the approach and reasonably cover the

North Pole. Orbit 9 (PJ9) was the last one in which JIRAM had a reasonably good coverage of the Pole. On the other hand, the South Pole could be observed almost during every perijove pass with good coverage and spatial resolution.

Table 1 provides a summary of the observations for which we were able to obtain good coverage of the polar regions: four for the North Pole and ten for the South Pole. Observations with more limited coverage have been excluded from this analysis. Given that Juno maintains a polar orbit of about 53 days, that is the minimum time interval between two successive observations reported here. The spatial resolution at the 1-bar pressure level is variable and ranges from about 15 km to about 60 km, depending on the position of the spacecraft in the orbit.

Date	Orbit #	Orbit type	Pole	Average Resolution	Images #
02/02/2017	4	MWR	North	51 km	9
			South	55 km	11
05/19/2017	6	MWR	North	23 km	45
			South	59 km	12
09/01/2017	8	GRAV	South	47 km	18
10/24/2017	9	MWR	North	39 km	40
			South	16 km	40
12/16/2017	10	GRAV	North	15 km	14
02/07/2018	11	GRAV	South	44 km	17
05/24/2018	13	GRAV	South	53 km	12
07/16/2018	14	GRAV	South	57 km	10
09/07/2018	15	GRAV	South	61 km	23
12/21/2018	17	GRAV	South	49 km	16
02/12/2019	18	GRAV	South	46 km	14

Table 1. Summary of the polar observations. The average resolution reported here is calculated at 1-bar level and it is referred to the mosaics shown in Figures 1, 2 and 3. It is the result of the resampling of the single images at a homogeneous spacing. Last column shows the number of images used for composing the mosaics of Figures 1,2 and 3.

In this paper we report and discuss the observations made by the JIRAM imager in band M of the CPC. Moreover, while tropospheric composition in hot spots and in extended regions at Jupiter's low and intermediate latitudes has been investigated by a number of authors on the basis of spacecraft and ground-based telescope data [e.g. Giles et al. 2015 and Giles et al. 2017], no study has yet covered the polar regions. However, starting from the Juno's fourth perijove (PJ4, February 2nd 2017) JIRAM has gradually acquired extensive observations over both poles. Here we calculate the tropospheric content of water, ammonia, phosphine and germane at Jupiter's polar regions from JIRAM spectral data in those areas where the atmospheric optical depth is less than 1.

Finally, in order to contribute to understanding of the dynamic processes that regulate the circumpolar structure of Jupiter we make comparisons with oceanic cyclones observed on Earth.

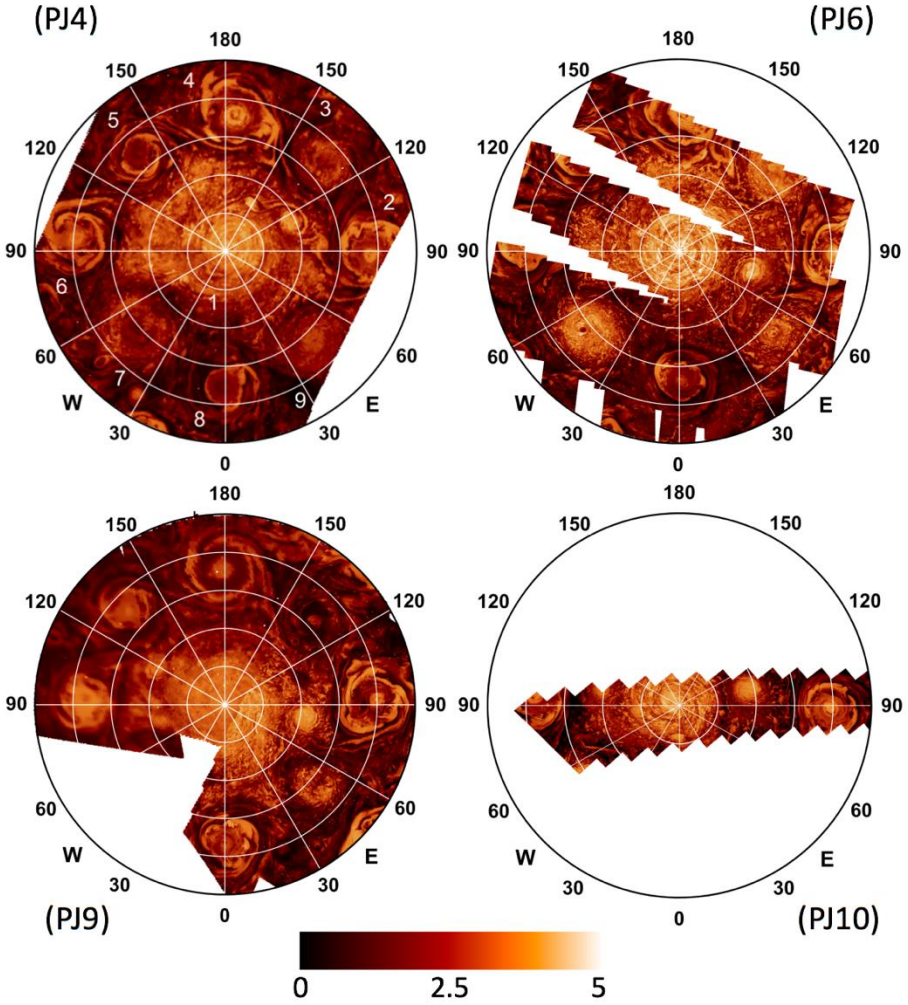

Figure 1. North pole during PJ4, PJ6, PJ9 and PJ10 (from top to bottom al left from right). Whitish colors indicate higher optical depth (τ), i.e. thicker clouds. Cyclone numbering: the polar cyclone is #1; the cyclone at 90E is #2; the numbering proceeds counterclockwise from #3 to #9. The color bar on the bottom indicates the value of τ.

2. Observations

Subsequent images acquired by JIRAM are composed in a single picture, called mosaic. Table 1 reports the pixel resolutions of the mosaics built by single stereographic maps based on System III longitude and planetocentric latitude coordinates and the number of images used for the relative mosaics. Mosaics are shown in Figures 1, 2 and 3: Figures 1 refers to the North Pole observations while Figures 2 and 3 refer to those at the South Pole. All the observations and the analysis reported here are at a latitude higher than 80°N and 80°S. All the single images used in this work, as well as the plots in the mosaics of Figures 1, 2 and 3, have been corrected by Beer's law, and the data were chosen so that the emission angle (the angle between the normal to the planet at the pixel location and the direction of the spacecraft) was always lower than 60° (except for the Northern cyclones #5 and #6 during PJ9). Figures 1, 2 and 3 are plotted in term of optical depth, $\tau = \log(I_0/I)$, that is normalized to the value I_0 = 0.65624 Wm^{-2} which is the maximum radiance measured at latitudes higher than 80° in both the north or in the south. In this scheme, light colors represent thicker clouds. That is, the figures show the cloudiness in the polar regions making them easier to compare to the visual camera observations of JunoCam, the camera onboard Juno. All JunoCam images

since the beginning of the mission are available on the Juno Mission website at https://www.missionjuno.swri.edu/junocam.

All the reported data have a geographical reference. We use NAIF-SPICE [Acton, 1996] and ENVI tools (by https://www.harrisgeospatial.com/Software-Technology/) for every geometric calibration and processing of images. Ultimately, the images in Figures 1, 2 and 3 are composites obtained by assembling different image sequences taken by JIRAM. They are plotted in geographic coordinates and show the maps of τ (as defined above) for the two poles. Significant differences between North and South are readily apparent from a visual comparison of Figure 1 versus Figures 2 and 3.

In Figure 1, we present the sequence of four North Pole observations summarized in Table 1. As stated previously by Adriani et al. [2018], the dynamic structure of this pole is shaped in such a way that the cyclones surrounding the polar one are approximately located on the vertices of a ditetragonal pattern. Some of the cyclones kept their cloud patchy structures in the eight months between PJ4 and PJ9, while others showed more clearly ordered cloudy spiral configurations with small cyclones or anticyclones inside the main structure. In general, the CPCs arrangement was quite stable during this entire period, and the internal structure of the single cyclones did not change significantly– including the one visible in PJ10.

Beside the small fluctuation of the CPCs around their average position, a big anticyclone was located around 87^{o}N latitude. It has been present since the first JIRAM observation during PJ4 (February 2017) and was still present during PJ10, a period slightly longer than 10 months. In this time span, it grew slightly in size from about 1,400 km up to about 2,000 km in diameter, oscillating between 80^{o}E and 120^{o}E longitudes in the "channel" between the polar cyclone and the circumpolar cyclones. Its changes in position can be clearly detected in Figure 1. Unfortunately, its later evolution could not be monitored due to the poor JIRAM coverage of the North Pole that resulted from the spacecraft attitude change during the remaining part of the mission.

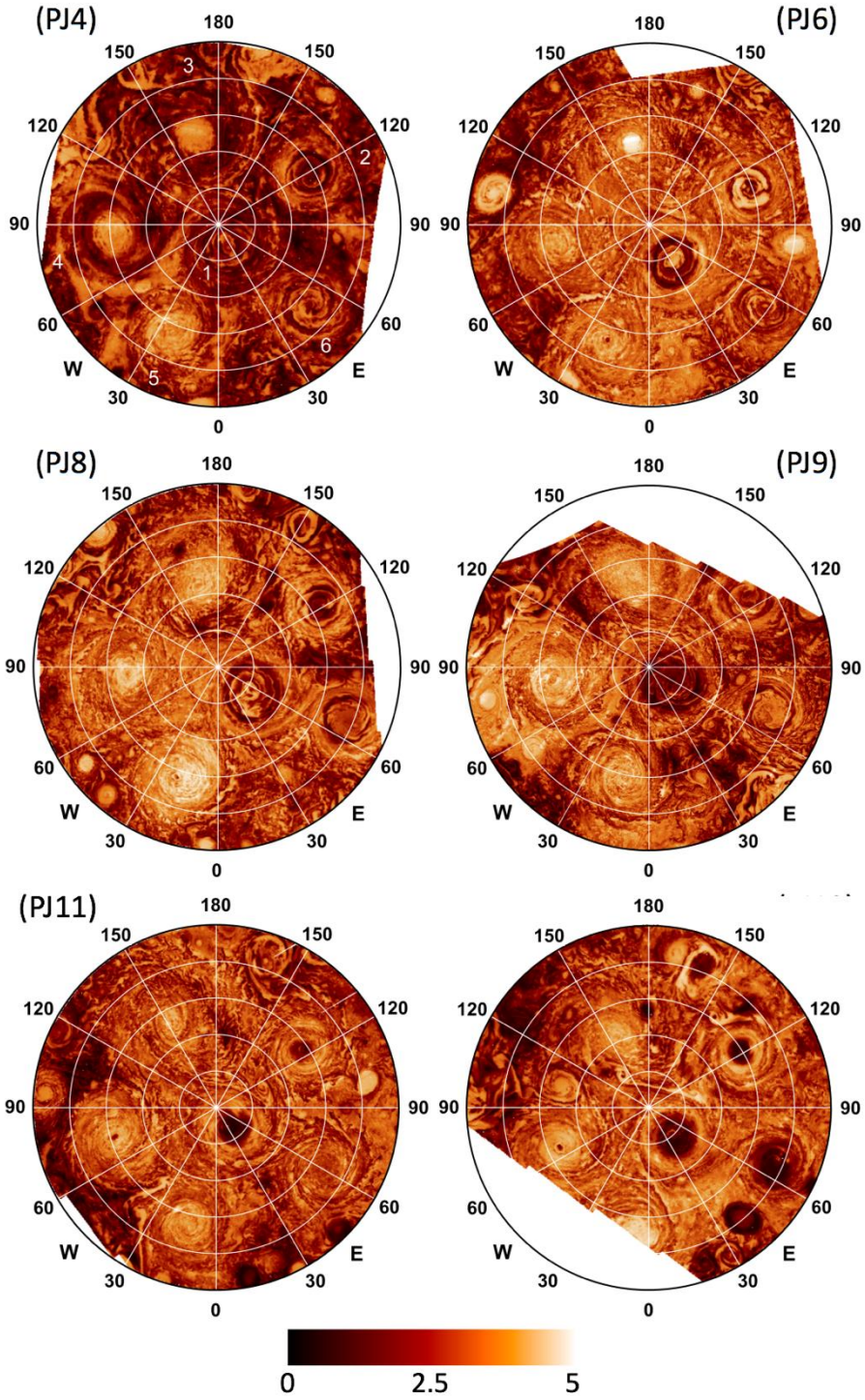

Figure 2. South pole from PJ4 to PJ13 (from top to bottom al left from right). Whitish colors indicate higher optical depth (τ), i.e. thicker clouds. Cyclone numbering: the polar cyclone is #1; the cyclone at the longitude of approximately 120E is #2; the numbering proceeds counterclockwise from #3 to #6. The color bar on the bottom indicates the value of τ.

In Figures 2 and 3 we present the sequence of ten South Pole observations summarized in Table 1. As already stated by Adriani et al. [2018] following the PJ4 observation in February 2017, the South Pole configuration is quite different from the northern one. The South Pole observations have continued on regular basis, and here we report about the evolution between PJ4 and PJ18. During a

time lapse of two years the pentagonal structure remained substantially unchanged, with only occasional perturbations.

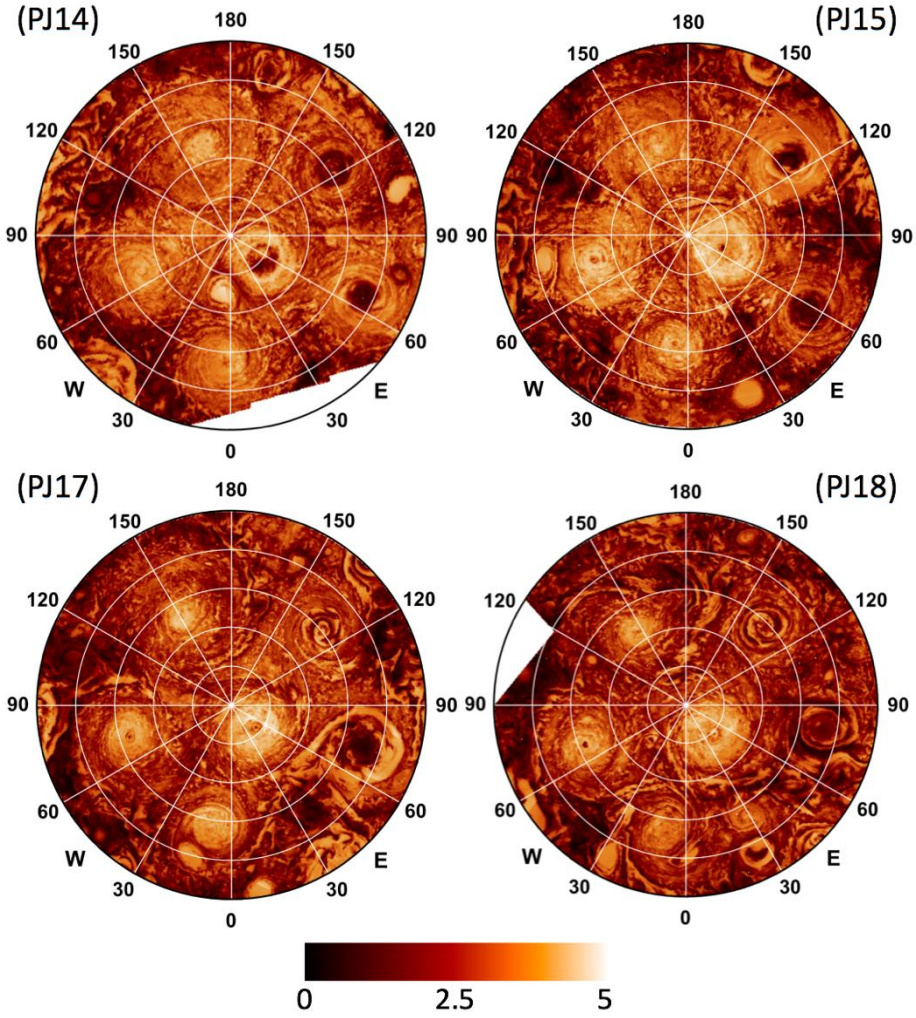

Figure 3. South pole during PJ14 to PJ18 (from top to bottom al left from right). Whitish colors indicate higher optical depth (τ), i.e. thicker clouds. Cyclone numbering: the polar cyclone is #1; the cyclone at the longitude of approximately 120E is #2; the numbering proceeds counterclockwise from #3 to #6. The color bar on the bottom indicates the value of τ.

As in the north, the six cyclones slightly changed their internal structure. In particular, as can be seen in Figures 2 and 3, the group formed by cyclones 3, 4 and 5 were more stable over the two-year period while the cyclones 1, 2 and 6 were more variable in terms of cloudiness. Unlike the North Pole, however, no long-lasting anticyclonic structures nested within the pentagonal structure were observed at the South Pole. During the first year, anticyclones appeared episodically within the cyclonic assembly but never lasted to the following perijove. On the other hand, a few relatively large anticyclones were present in the second year of the mission, from PJ13 onward. Moreover, toward the end of the period a new feature appeared between the CPCs #5 and #6 (see Figure 4 for the identification of CPC numbers). This structure is reminiscent of a vortex dipole whose embryo

was already recognizable during PJ15. During PJ18 the Southern CPCs appeared to move to a hexagonal shape where the new-born vortex is joining the previous ones around the central cyclone.

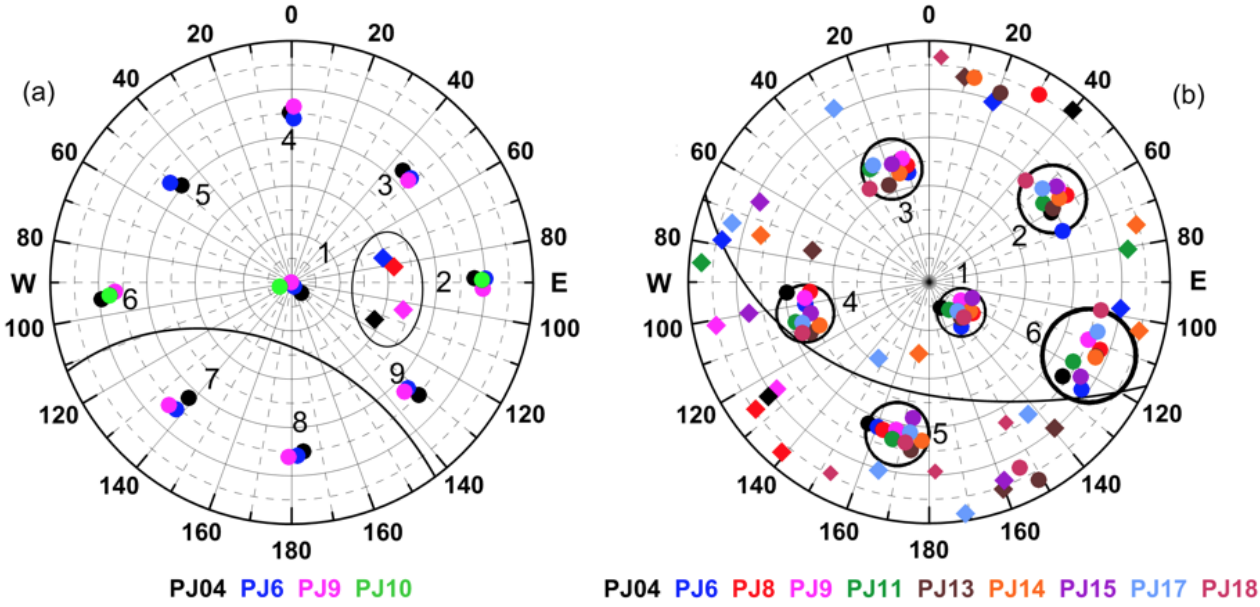

Figure 4. Position of the cyclone centers (dots) during the observation period for North pole [panel (**a**)] and South pole [panel (**b**)]. The colors identify the different perijoves. The black circles indicate the variation of the position of the southern cyclone centers and are centered at the average position measured in the all period of observations. The diamonds represent the position of the different anticyclones with diameters larger than 1000 km. The oval in panel (**a**) identify the different positions **of** the same anticyclone during the different reported perijoves.

Figure 4 illustrates the position of the cyclones and the anticyclones with diameters larger than 1000 km observed in the polar region of both hemispheres. In the almost 9 months during which we could get good coverage of the North Pole no anticyclones of sizes larger than 1000 km were observed at latitudes higher than 80^{o}N beside the one hovering at 87^{o}N between the NPC and the CPCs. On the other hand, a large number of anticyclones were observed in the southern regions, particularly at longitudes between 100^{o}E and 300^{o}E. Most of them appeared to be connected to a cyclone in a dipole configuration. Sometimes the cyclone was one of the CPCs, as in the case of CPC#5 where the anticyclone was still present during PJ19 (not shown here). During PJ18, CPC#6 moved significantly towards lower longitudes leaving space for the intrusion of a cyclone/anticyclone dipole that could anticipate the formation of a new CPC. Other cyclones with diameters larger than 1000 km occasionally grew outside the CPCs ring, but they never appeared to last for more than a 53-day perijove pass.

The average radiances measured in the spectral range 4.5-5.0 μm are systematically higher in the north than in the south. In the north the average value is 0.133 Wm-2, while in the south the average is 0.069 Wm-2 [Figure 5 panel (a)]. During PJ4 the southern radiance was at its highest value of 0.1 Wm-2 followed by an abrupt decay of about 50% during PJ6, after 106 days.

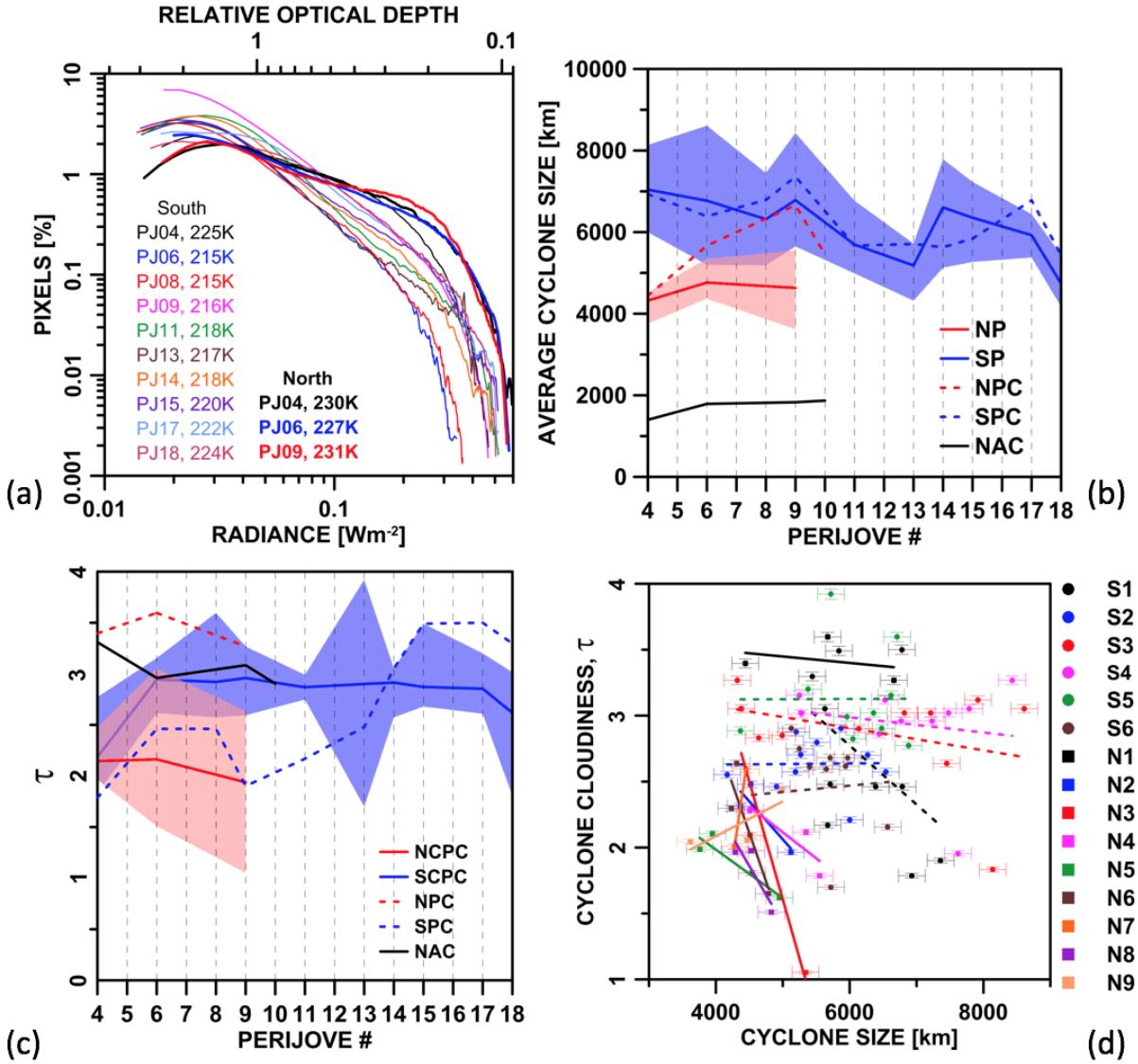

Figure 5. (**a**): Distribution of pixels radiance, the average brightness temperature at latitudes higher than 80° is given for each perijove. (**b**): The blue and the red curves gives the average diameter of the circumpolar cyclones for the south and the north respectively; the dashed curve account for the respective polar cyclones; the blue and the red areas show the minimum to maximum variation of the cyclones size; the black curve gives the diameter of the only larger anticyclone observed in the north; (**c**): optical depth of cyclones, following the color definitions for panel (b). (**d**): optical depth versus cyclone size; in the legend S stands for south and N for north and the numbering criterion is the same given in figures 1, 2 and 3.

A slow but progressive increase has been observed after PJ6 [see Figure 4 panel (a) for details]. Panel (a) of Figure 5 shows also the statistics of the pixels' brightness of the two poles in terms of radiance. In the legend, the corresponding average brightness temperature for each PJ and at latitudes higher than 80° N/S is also given. A direct comparison between North and South can be only done for the first year, as no north pole images in the infrared range are available after December 2017.

Some single cyclone characteristics have been investigated in order to monitor the changes that occurred in the two years of observations, from February 2017 to February 2019. Figure 5 also accounts for changes in the average diameters [panel (b)] and cloudiness [τ, in panel (c)] of the

single cyclones versus time from PJ4 to PJ18. The diameters of the northern and southern cyclones are substantially different. The average diameter of the northern cyclones is about 4,600 km. Southern cyclones, being fewer than but occupying approximately the same latitudinal extension as the northern ones, are systematically larger, their average diameter reaches approximately 6,300 km. Another difference between south and north is the relative size of the polar cyclone with respect the surrounding CPCs. While the size of the southern polar cyclone (SPC) is commensurate with the surrounding CPCs, the northern one (NPC) is significantly larger than its surrounding CPCs [see panel (b) of Figure 5]. Focusing on the time evolution of southern cyclones' sizes, we note both a general decrease and a sort of pulsation in the distribution of the dimensions: namely, sometime the cyclones are quite different from each other, but at other times their sizes are more similar. Also, from the cloudiness point of view, the NPC differs from the surrounding cyclones showing an average τ of 3.4 while its CPCs have an average value of 2.1. The opposite happens for the SPC whose cloudiness ($\tau \approx 2.2$) is systematically lower than the average cloudiness of the surrounding CPCs ($\tau \approx 2.8$). The SPC cloudiness grows significantly reaching values similar to the NPC during the last part of the time period analyzed. Finally, in general, the cyclones are characterized by the tendency to reduce or maintain more or less their cloudiness when growing in size [see panel (d) of Figure 5]. In a couple of cases we observed the opposite behavior.

3. Spectral Analysis

To get more insights on the behavior of the CPC we have used the spectra recorded by JIRAM to obtain the atmospheric and cloud composition in relatively clear areas in the polar regions. The performed spectral analysis is limited to the wavelength range between 4 and 5 μm and considers only the thermal emission of the planet. This enables to monitor in the same way the atmosphere both when illuminated and when not illuminated by the sun. In fact, , in the brightest areas examined in our work the scattered solar contribution in the 4-5 μm region is expected to be

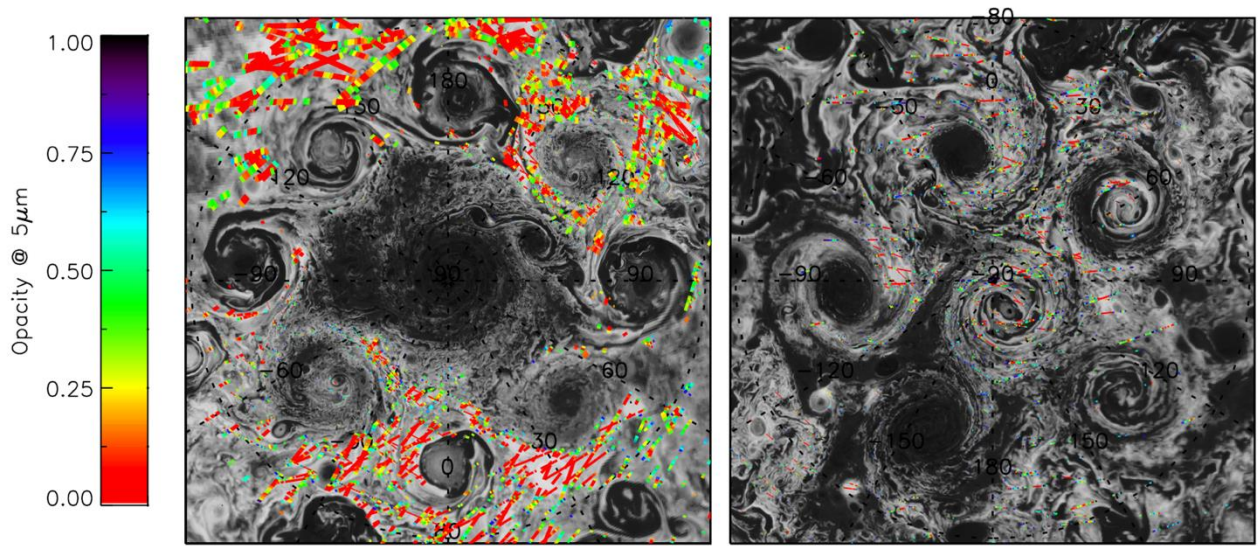

between 100 and 800 times smaller than the thermal component, as previously reported by Drossart et al. [1998].

Figure 6. Areas where the optical depth, in the infrared wavelengths around 5 μm, is lower than 1 according to the JIRAM spectrometer data.

Most of the polar regions of Jupiter are affected by thick cloud coverage but relatively clear areas (with cloud total opacities < 1 at 5 μm) exist at some specific locations, similar to the hot spots frequently observed between the Equatorial Zone and the North Equatorial Belt [Grassi et al. 2017a]. Figure 6 shows the polar areas within 80°N/S latitudes where the optical depth, τ, is lower than 1 at PJ4. Correspondingly, Figure 6 shows the areas where the JIRAM spectra are sensitive to the contents of ammonia, water vapor, phosphine and – in lesser degree – germane, at the approximate levels between 2 and 3 bar [Grassi et al. 2017b], well below Jupiter's tropopause level. Water and ammonia are condensable and involved in the cloud formation while germane and phosphine are disequilibrium species from the deep interior and they are retrievable from JIRAM spectral data in the range 4.5-5. μm.

The set of parameters to be retrieved has been defined following the scheme already proposed in Irwin et al. [1998] for hot spots. The adopted scheme aims to distinguish, where relevant, the 'deep' content of gaseous species from their mixing ratios in the upper troposphere, where depletion may occur due to condensation or photochemistry. According to that scheme, for the analysis here, we consider different free parameters: H_2O, NH_3, PH_3, and GeH_4 "deep" mixing ratios, which are all assumed to be constant with altitude; the H_2O relative humidity above its condensation level and constant with altitude; and the total optical depth at 5μm of the main (putative NH_4SH) cloud above the water cloud. The topmost cloud layer (putatively NH_3) is thought to be essentially absent in hot-spot regions, while diffuse haze has been demonstrated to be transparent at 5μm.

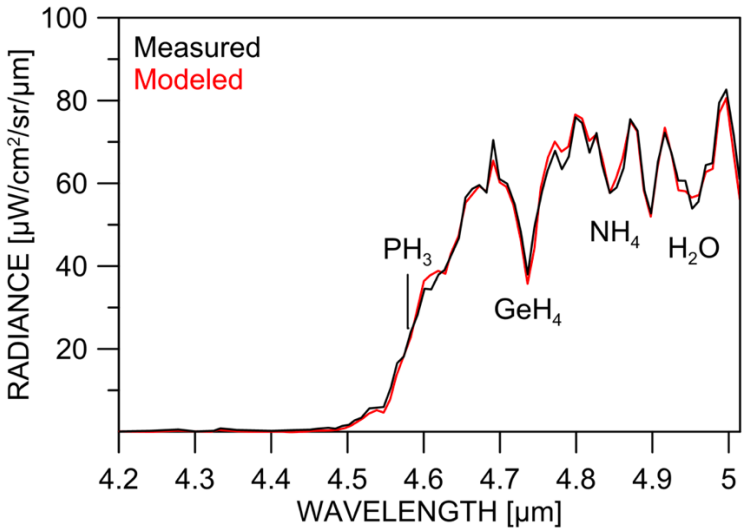

Figure 7. Comparison between a measured and a reconstructed spectrum between 4.2 and 5 μm

Figure 7 displays the spectral region used for the retrieval. It also shows how the model used in the retrieval is able to reproduce the measured spectrum. Performance of the retrieval code has been quantified on the basis of test runs on large sets of simulated observations and the retrieval errors include the effects of forward-modelling errors in the radiative transfer. Notably, these errors exceed by at least a factor of 10 the instrumental Noise Equivalent Radiance, as estimated in Adriani et al. [2016]. Considering the typical nominal values of retrieval errors and assuming a mean deterioration factor 5 for all gases, we can estimate the approximate uncertainties for the retrieved contents of different gases from individual spectra as follows: $Log_{10}([H_2O]_{RH}) \sim 0.08$, [NH3] ~ 30 ppm, [PH3] ~ 60 ppb and [GeH4] ~ 0.043 ppb. As water vapor is by far the most variable gas in the Jupiter atmosphere, it is more appropriate to express its abundance using the logarithm of relative humidity (i.e.: the original state vector element in our retrieval code) rather than use the mixing ratio.

Our retrieval model uses the temperature-vs-pressure profile from Seiff et al. [1998] on the basis of the Galileo Entry Probe measurements. In order to quantify errors introduced by possible variations of the real temperature with respect to the assumed value, numerical tests demonstrate that a systematic increase or decrease of 5K at every fixed pressure level of our atmospheric model induces a relative variation of about 2% in the retrieved contents of ammonia and phosphine, of 5% in germane and 15% in the water relative humidity value.

The analysis presented here was performed on PJ4 data (February 2nd, 2017). The method is described in more detail by Grassi et al. [2017b] and the analysis is restricted to spectra with low emission angle to limit retrieval uncertainties and attain higher signal.

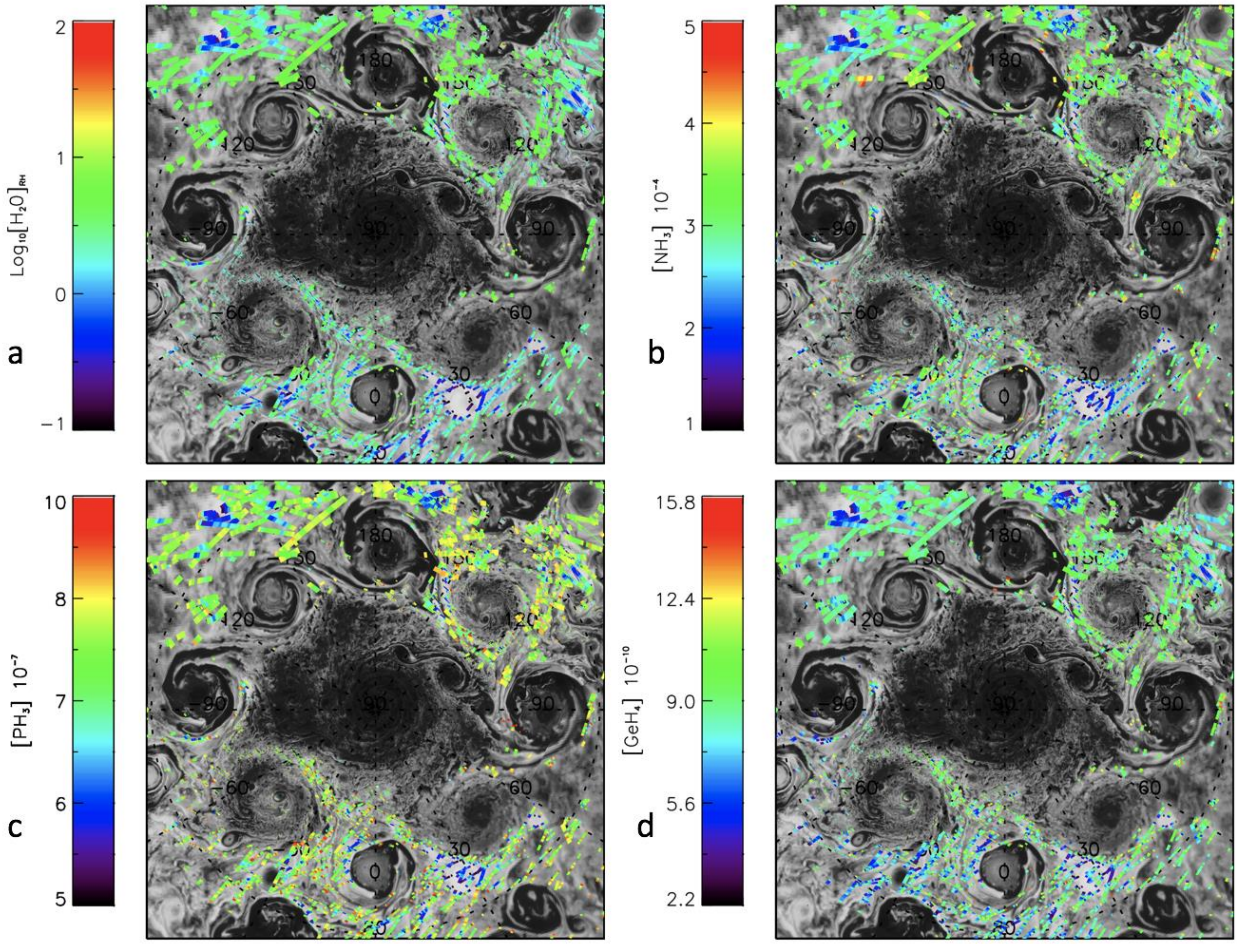

Figure 8. North pole maps of water relative humidity (**a**), ammonia (**b**), phosphine (**c**) and germane (**d**) concentrations.

Results of the analysis are reported in Figures 7 and 8 for the relative humidity of water vapor and the concentrations of ammonia, phosphine and germane, for the North and South Poles, respectively. The thickness of the tracks is proportional to the pixel resolution at Jupiter's 1-bar level. It is noticeable that the abundances of condensable species (H_2O and NH_3) are more depleted over the lower-opacity regions. However, those gases appear r**el**atively enhanced over the South Pole compared to northern regions, possibly because of smaller overall opacity of cyclones in the former areas during Juno PJ4 passage. Values range between 0.3% and 10% for the water vapor relative humidity and between 100 and 500 ppm for the ammonia mixing ratio in the north (see

Figure 8), and between 0.3% and 20% for both for the water vapor relative humidity and ammonia in the south, but with an average significantly shifted toward the upper value (see Figure 9).

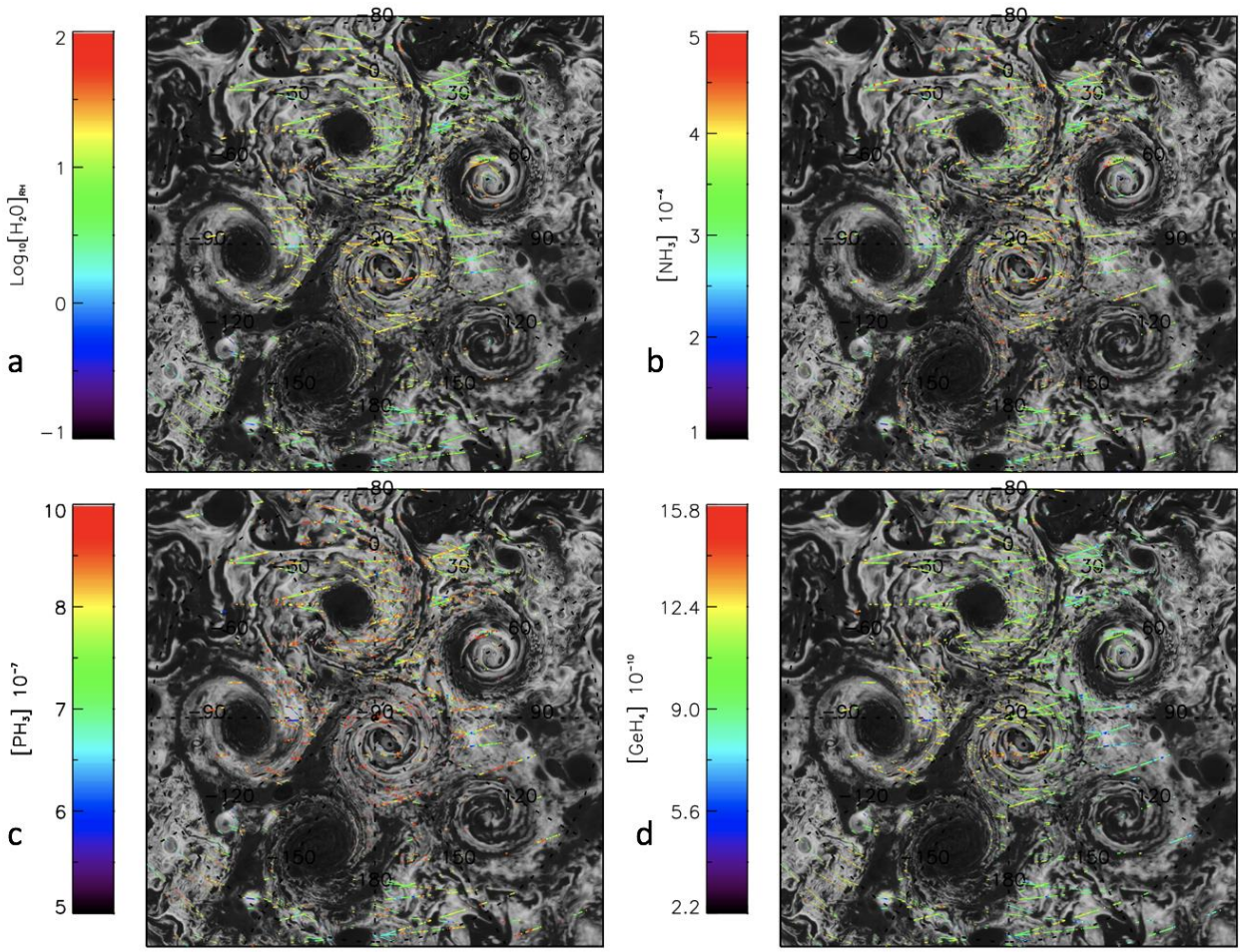

Figure 9. South pole maps of water relative humidity (**a**), ammonia (**b**), phosphine (**c**) and germane (**d**) concentrations.

Areas with the lowest cloud cover are found to be considerably depleted in disequilibrium species (PH_3 and GeH_4) once compared against moderately cloudy ones, suggesting effective suppression of vertical upwelling (see Figures 7 and 8). PH_3 has abundances of the order of 0.6-1 ppm in the north while it reaches up to 2 ppm in the south. Also the GeH_4 shows the same difference between north and south with values of 6-10 ppb values that reach 15 ppb respectively. However, the comparison of absolute values between the two poles must also consider the better spatial resolution of the southern spectra for most of the JIRAM data, capable therefore of singling out more extreme values.

PH_3 and GeH_4 are not stable at the pressure and temperature conditions of the upper troposphere where they are detected. They are usually interpreted as tracers of active vertical motions that replenish the upper levels with fresh material from the much deeper atmosphere, where they are in equilibrium. The concentration contrasts between bright and dark area appear stronger over the

northern pole and the depletion of germane looks stronger than for phosphine (see Figure 10). The ratio $[PH_3]/[GeH_4]$ is of order a thousand.

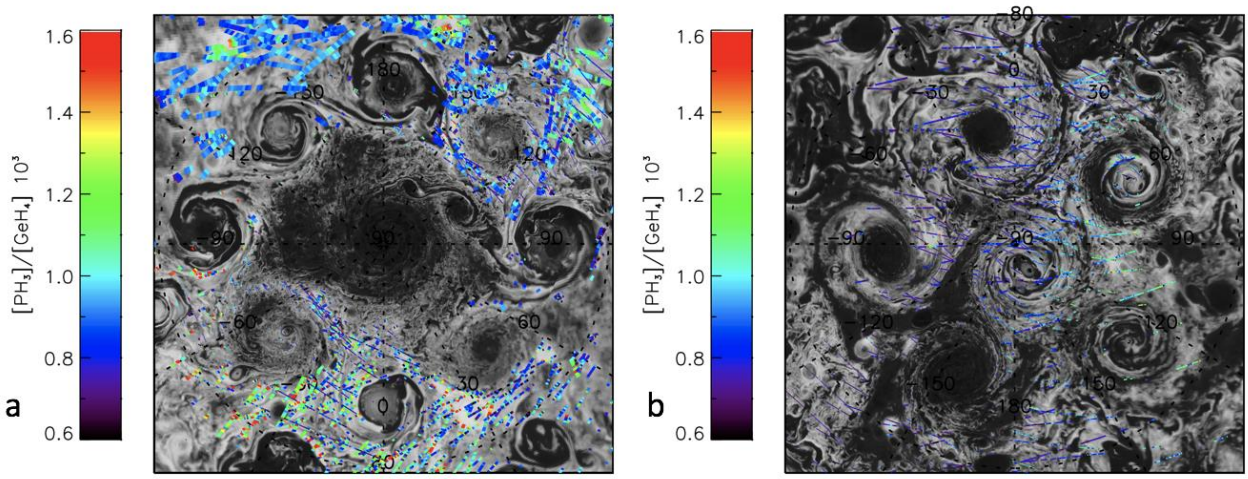

Figure 10. Maps of phosphine to germane ratio for the North (left panel) and for the South (right panel)

4. Dynamics

The process of mosaicking, as seen in Figures 1, 2 and 3, can alter the original images as a re-pixelization process is necessary to create maps. Because of the lowering of the orbit over North Pole, we achieved a resolution better than 16 km for some of the images during PJ9 pass. From a visual analysis of those images, the existence of wavy structures over some parts of the polar cyclones could be conjectured. In fact, a more sophisticated analysis by using 2D Fourier filtering to highlight short- wavelength (high-frequency) perturbation has been applied to some of the single images not affected by image processing. The analysis revealed the presence of many wavy structures hovering near some part of the cyclones. This topic is better described by Moriconi et al. [2019] but an example is given in Figure **11** where the upper panel shows one of the original images taken by JIRAM approaching the northern CPC#2. A 2D Fourier filtering applied to the image provides the result illustrated in the second panel where the full wavy structure has been isolated from the image background. The result indicates a strong dynamical interaction between the lower level, where presumably the top of the cyclones is, with the higher levels of the troposphere. The upper level waves appear to have a typical wavelength of about 20-30km. The wavy perturbations may be induced by the ascending currents in some areas of cyclones that perturb the atmosphere above the cyclones, or they could result from the interaction of the surface wind field with the vortex population, analogously to Langmuir turbulence in the upper turbulent layer of Earth's oceans, the so-called ocean mixed-layer [Hamlington et al., 2014].

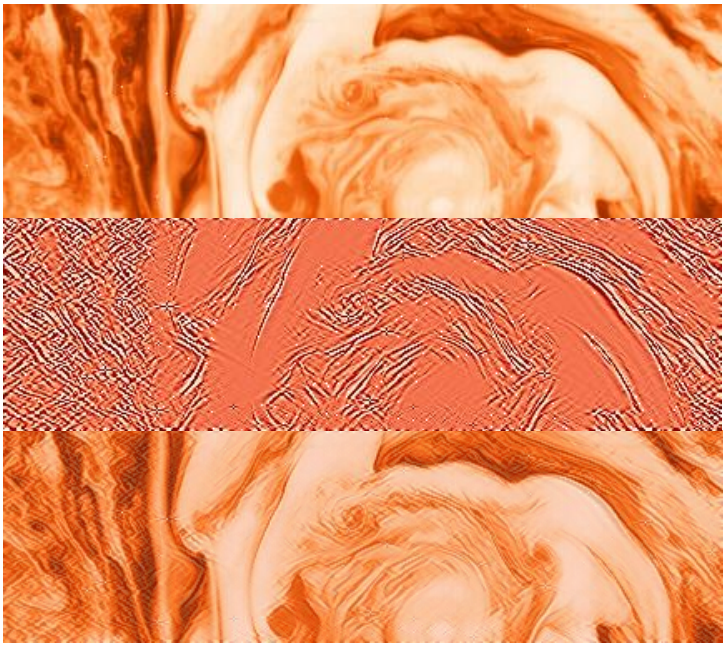

Figure 11. Waves over the cyclone #2 at the North Pole. Upper panel: original JIRAM image; central panel: result of the 2D Fourier high-pass filtering on the original image; lower panel: superimposition of the central panel to the upper panel.

A more in-depth analysis to understand the structure of the polar cyclones has been performed by attempting a comparative power spectrum investigation of long-living mesoscale (~100 km diameter) cyclones in Earth's ocean. In fact, the semi-stable, turbulent instabilities observed at Jupiter's Poles within and around the patterns of cyclones are reminiscent of the dynamics and instabilities observed in the buoyancy distributions in the Earth's oceanic mixed-layer [McWilliams, 2016] or in the potential temperature anomalies in the upper tropopause [Hakim et al. 2002]. In the ocean, these instabilities develop at scales smaller than the local Rossby deformation radius, between few hundred meters and 2-3 km, and contribute to the internal structure of mesoscale vortices and to very large vertical velocities and intense vertical exchanges [e.g Zhong et al., 2017]. They are associated **with** the development of fronts at scales where the planetary rotation is still important but not dominant, and are characterized by intense vertical velocities [McWilliams, 2016].

The emergence of these kilometer-scale fronts cannot generally be described by quasigeostrophic (QG) models, developed by Charney [1971] to describe in a conceptually simple, two-dimensional framework, the dynamics of atmospheric and oceanographic flows with horizontal length scales which are very large compared to their vertical extension whenever the strength of inertia is small compared to the strength of the Coriolis force. On the other hand, the laterally divergent flows associated with frontogenesis are approximated in two-dimensions whenever the QG model is applied to a semi-infinite domain with zero potential vorticity (PV) in the interior. In this special case the so-called Surface Quasi-Geostrophy (SQG) approximation, first introduced by Blumen [1978] assumes that the flow evolution is controlled by the advection–diffusion of surface buoyancy at the boundary. It is based on the conservation of this active scalar (surface buoyancy) along the horizontal geostrophic flow, and links velocity and buoyancy.

The SQG model has shown some success in interpreting turbulent dynamics in the troposphere [Held et al. 1995], the dominance of cyclones over anticyclones at the tropopause [Hakim et al. 2002], and more recently, observations in the oceanic mixed-layer [Lapyere and Klein, 2006].

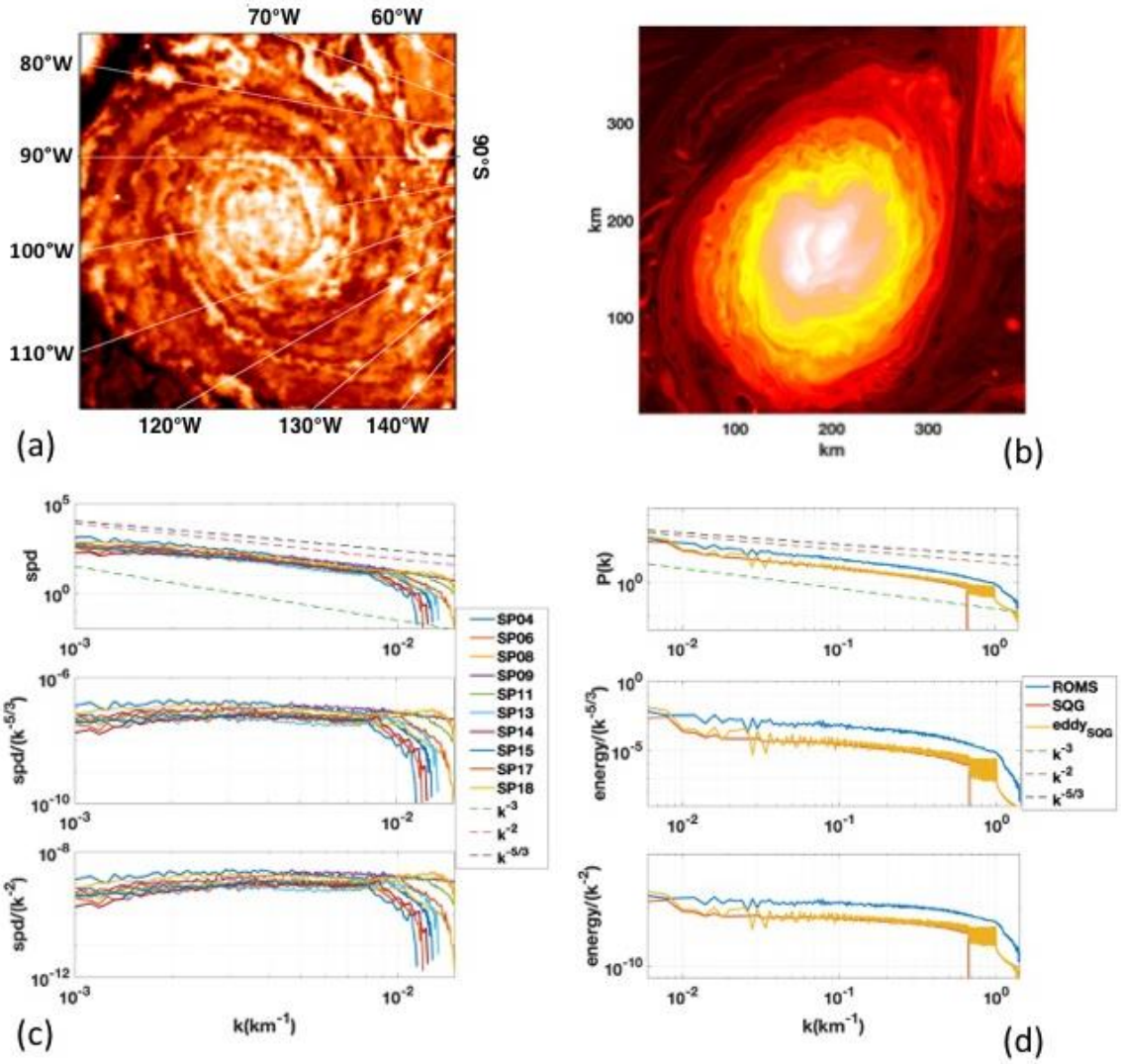

Figure 12. (**a**) Jupiter cyclone #4 from South Pole PJ4 image. (**b**) Cyclonic eddy in surface buoyancy in a freely-decaying SQG simulation at a resolution of 1024 x 1024. Several Gaussian shaped cyclones are seeded as initial conditions in a freely-decaying, unforced run. The figure shows one of the remaining cyclones after approximately 50 rotation periods. (**c**) 2D power spectra for selected data sets from Jupiter South Poles; the power spectra calculated for Jupiter are related to the latitudes higher than 82°S that are dominated by the presence of the polar cyclones. (**d**) 2D power spectra for the cyclone in panel (b) in light orange, for the whole SQG field at the time the cyclone was extracted in dark orange, and for an ocean cyclonic eddy obtained by ROMS run in the Gulf Stream region at horizontal resolution of 750 m [courtesy of J. Gula]. The ocean cyclone is approximately 200 km in diameter and the non-dimensional SQG eddy has been scaled to match it.

One characteristic that sets apart SQG, and flows in the oceanic mixed-layer, from "traditional" QG and two-dimensional turbulent flows is the slope of the energy power spectra, which is shallower than the non-local $E(k) \propto k^{-3}$ predicted for two-dimensional and QG systems in the direct cascade range [e.g. Bracco et al., 2004; Bracco and McWilliams, 2010]. An energy spectrum as steep or

steeper than k^{-3} is indicative of non-local dynamics, where coherent, large scale vortices dominate. The theoretical SQG slope of buoyancy variance in the direct energy cascade range is indeed $\propto k^{-5/3}$, indicative of local dynamics, where frontal and filamentary structures at scales smaller than the large coherent vortices control mixing. These local dynamics are behind the large vertical velocities and their localization in circulations of scales smaller than the Rossby deformation radius of the flow. Numerical simulations in various configurations using both the SQG approximation, or the primitive equations commonly employed by ocean models, concur in finding spectral slopes slightly steeper than $k^{-5/3}$ and usually approaching k^{-2} [Pierrhumbert et al., 1994; Held et al., 1995; Capet et al., 2008; Zhong and Bracco, 2013]. The steepening of the theoretical slope is commonly found in presence of large vortices, but could also be related to numerical diffusion.

In Figure 12, the power spectra calculated on the full two-dimensional image mosaics return slopes consistent with the SQG model. The analysis done here follows the empirical correspondence between power spectra of atmospheric kinetic energy and those of cloud opacities as shown by Harrington et al. [1996] for Jupiter, on the basis of Travis [1978] previous results on Venus and Earth. Travis, in fact, found a close correspondence between power spectra of atmospheric kinetic energy and power spectra of visible and infrared cloud intensities. The same figure shows an eddy obtained integrating the SQG equation using a pseudo-spectral code and resolution 1024 x 1024 grid points over a 2π x 2π non-dimensional domain; the eddy occupies nearly 1/4 of the model domain. The cyclone's energy spectra are shown with that of the whole domain including two more cyclonic eddies, and the spectrum of an upper ocean cyclone simulated by the Regional Ocean Modeling System [ROMS, Shchepetkin and McWilliams, 2005] at 750 m horizontal resolution [Gula et al., 2015].

The power spectra consistency is supported by a visual similarity, but other turbulent systems are characterized by analogous slopes. For example, recent work [Novi et al. 2019] has shown that rapidly rotating convective flows can generate intense vortices close to the poles on a spherical planet in local Cartesian approximation. These convective flows also have slopes close to k^{-2} but the structure of convective plumes and their vertical velocities appear to be more disorganized within the eddy [see, for a convective cyclonic plume in the high latitude Earth's ocean, Fig. 4 in Sun et al., 2017].

5. Conclusions

Jupiter's polar cyclonic structures on both northern and southern polar regions show no considerably changes during the two years of JIRAM observation considered in this study (February 2017 - February 2019). Differences between Jupiter's North Pole and South Pole are evident not only by counting the number of persistent cyclonic structures or the anticyclonic activity but also by other properties such as cloudiness, size, and concentration of minor and trace atmospheric species such as water vapor, ammonia, phosphine and germane. The question is whether these differences are only the consequence of an evolution of the two polar zones that proceeds on different time scales or, instead, there is a persistent and more profound connection with the deepest part of the Jovian atmosphere, such as its magnetic field which results to have a very different structures between north and south. In relation to the stability of the vortex configurations found at Jupiter's poles, Reinaud [2019] recently investigated the conditions under which an array of *m* three-dimensional, unit Burger number, quasi-geostrophic vortices on a ring, with an additional vortex lying on the array center, are in mutual equilibrium. He found that the central vortex, if moderate in strength and having the same rotation sign of the peripheral ones,

stabilizes the vortex array for a long time in a QG system. He refers specifically to the cluster of cyclones of Jupiter's polar regions as an example of environmental context where his study can be applied. On the other hand, our comparative analysis shows similar results for cyclones in both the Jupiter and the Earth's case cyclone in the upper ocean mixed-layer, with the size of the cyclones being proportional to the size of the planet to which they belong to. It also suggests the possibility of a well-mixed upper boundary layer on Jupiter's Poles with the cyclones being key mediators of any exchange with deeper layer(s) though large vertical velocities localized in frontal regions that result from local, non-geostrophic dynamics. Indications of the possible presence of fronts come from the strong gradients in optical depth and small scale structure in and around the cyclones. Finally, although our work on JIRAM data has provided insights into the dynamics of Jupiter's polar regions, additional measurements from Juno's other instruments, like the Juno's MicroWave Radiomenter (MWR) which is able to sound deeper in the atmosphere, and corresponding analyses are necessary to explain the origin of Jupiter's curious polar cyclones.

Acknowledgements and Data

This work was supported by the Italian Space Agency through ASI-INAF contract I/010/10/0 and 2014-050-R.0.

AA, DG, MLM, AMu, FA, AMi, RN, AC, RS, GS, CP, BMD, AT, GF, GP, and FT were supported by ASI. GO was supported by NASA with funds distributed to the Jet Propulsion Laboratory, California Institute of Technology. AI, SKA, JIL, and SJB were supported by the Juno Project.

The JIRAM instrument was developed by Leonardo at the Officine Galileo - Campi Bisenzio site.

The data used for this study will be available once the proprietary period ends from the NASA's Planetary Data System at https://pds.jpl.nasa.gov/tools/data-search/.

References

Acton, C.H. (1996). Ancillary data services of NASA's Navigation and Ancillary Information Facility *Planetary and Space Science*, 44, 65-70, doi: 10.1016/0032-0633(95)00107-7

Adriani, A., et al. (2016) Juno's Earth flyby: the Jovian infrared Auroral Mapper preliminary results. Astrophysics and Space Science, 361 (8), article id.272.

Adriani, A., Mura, A., Orton, G., Hansen, C., Altieri, F., Moriconi, M.L., Rogers, J., Eichstädt, G. et al. (2018). Clusters of Cyclones Encircling Jupiter's Poles. *Nature*, 555, 216-219, doi: 10.1038/nature25491

Adriani, A., Filacchione, G., Di Iorio, T., Turrini, D., Noschese, R., Cicchetti, A., Grassi, D., Mura, A., et al. (2017). JIRAM, the Jovian Infrared Auroral Mapper. Space Science Reviews, 213, 393-446, doi: 10.1007/s11214-014-0094-y

Blumen, W. (1978). Uniform potential vorticity flow: Part I. Theory of wave interactions and two-dimensional turbulence. *Journal of Atmospheric Science*, 35, 774–783.

Bolton, S.J., Lunine, J.I., Stevenson, D., Connerney, J.E.P., Levin, S., Owen, T. C., Bagenal, F., Gautier D., et al. (2018). The Juno Mission. *Space Science Reviews*, 213, 5-37, doi: 10.1007/s11214-017-0429-6.

Bracco, A. & McWilliams, J.C. (2010). Reynolds-number dependency in homogeneous, stationary two-dimensional turbulence. *Journal of Fluid Mechanics*, 646, 517-526.

Bracco A., J von Hardenberg, A. Provenzale, J. Weiss & J.C. McWilliams (2004). Dispersion and mixing in quasigeostrophic turbulence, *Physical Review Letters*, 92, 084501-1 - 4

520 Capet X., Klein P., Hua B.L. Lapeyre, G., & McWilliams J.C., (2008), Surface kinetic and potential
521 energy transfer in SQG dynamics. *Journal of Fluid Mechanics*, 604, 165–174.

522 Charney, J.G. (1971). Geostrophic turbulence. *Journal of Atmospheric Science*, 28, 1087–1095, doi:
523 10.1175/1520-0469(1971)028<1087:GT>2.0.CO;2

524 Drossart, P., et al. (1998) The solar reflected component in Jupiter's 5-μm spectra from
525 NIMS/Galileo observations, J. Geophys. Res., 103 (E10), doi:10.1029/98JE01899

526 Giles, R.S., Fletcher, L.N., & Irwin P.G.J. (2015). Cloud structure and composition of Jupiter's
527 troposphere from 5-m Cassini VIMS spectroscopy, *Icarus*, 257, 457-470,
528 doi:10.1016/j.icarus.2015.05.030.

529 Giles, R.S., Fletcher, L.N., & Irwin P.G.J. (2017). Latitudinal variability in Jupiter's tropospheric
530 disequilibrium species: GeH4, AsH3 and PH3, *Icarus*, 289, 254-269,
531 doi:10.1016/j.icarus.2016.10.023.

532 Grassi, D., Adriani, A., Mura, A., Dinelli, B.M., Sindoni G., Turrini D., Filacchione, G., Migliorini,
533 A., et al (2017a). Preliminary results on the composition of Jupiter's troposphere in hot spot
534 regions from the JIRAM/Juno instrument. *Geophysical Research Letters*, 44 (10), 4615-
535 4624, doi:10.1002/2017GL072841.

536 Grassi, D., Ignatiev, N.I., Sindoni, G., D'Aversa E., Maestri T., Adriani, A., Mura, A., Filacchione,
537 G., et al (2017b). Analysis of IR-bright regions of Jupiter in JIRAM-Juno data: Methods
538 and validation of algorithms. *Journal of Quantitative Spectroscopy and Radiative Transfer*,
539 202, 200-209, doi:10.1016/j.jqsrt.2017.08.008.

540 Gula, J., Molemaker M.J. & McWilliams, J.C. (2015). Gulf Stream dynamics along the
541 southeastern U.S. Seaboard. *Journal of Physical Oceanography*, 45, 690–715,
542 doi:10.1175/JPO-D-14-0154.1.

543 Irwin, P.G.J., Weir, A.L., Smith, S.E., Taylor, F.W., Lambert, A.L., Calcutt, S.B., Cameron-Smith,
544 P.J., Carlson R.W., et al. (1998). Cloud structure and atmospheric composition of Jupiter
545 retrieved from Galileo near infrared mapping spectrometer real-time spectra. *Journal of*
546 *Geophysal Research Planets*, 103 (E10), 23001-23021, doi:10.1029/98JE00948.

547 Hakim G.J., Snyder C. and Muraki D. J. (2002), A new surface model for cyclone–anticyclone
548 asymmetry. *J. Atmos. Sci*., 59, 2405–2420.

549 Hamlington P.E., Van Roekel P., Fox-Kemper B. et al. (2014), Langmuir–Submesoscale
550 Interactions: Descriptive Analysis of Multiscale Frontal Spindown Simulations. J. Physic.
551 Ocean., 44, 2249-2272, doi:10.1175/JPO-D-13-0139.1.

552 Hansen, C.J. et al. (2014). Junocam: Juno's Outreach Camera, Space Sci. Rev. doi 10.1007/s11214-
553 014-0079-x.

554 Harrington J., T.E. Dowling, and R.L. Baron (1996). Jupiter Tropospheric Thermal Emission: II.
555 Power Spectrum Analysis and Wave Search. Icarus, 124, 32-44, doi:
556 10.1006/icar.1996.0188

557 Held I.M., Pierrehumbert R.T., Garner S.T., et al (1995), Surface quasi-geostrophic dynamics. J.
558 *Fluid Mech.* 282, 1–20.

559 Lapeyre G. and Klein P. (2006), Dynamics of the upper oceanic layers in terms of surface
560 quasigeostrophy theory. *J. Phys. Oceanogr*., 36, 165–176.

561 McWilliams JC. (2016), Submesoscale currents in the ocean. *Proc. R. Soc. A* 472: 20160117,
562 http://dx.doi.org/10.1098/rspa.2016.0117

563 Moriconi M.L., A. Migliorini, F. Altieri, et al. (2019), Power spectrum analysis of Jupiter's polar
564 clouds by Juno/JIRAM data, submitted to *JGR* Planets.

565 Pierrehumbert, R.T., I.M. Held and K.L. Swanson (1994) Spectra of local and nonlocal two-
566 dimensional turbulence. *Chaos, Solitons, Fractals* 4, 1111–1116.

567 Reinaud J.N. (2019), Three-dimensional quasi-geostrophic vortex equilibria with m-fold symmetry,
568 J. Fluid Mech., 863, 32_59, Cambridge University Press 2019, doi:10.1017/jfm.2018.989

569 Seiff, A. et al. (1998) Thermal structure of Jupiter's atmosphere near the edge of a 5-μm hot spot in
570 the north equatorial belt, J. Geophys. Res., 103 (E10), doi:10.1029/98JE01766. Available as
571 numerical data as GP-J-ASI-3-ENTRY-V1.0, NASA Planetary Data System.

572 Shchepetkin A.F., and J.C McWilliams JC. (2005), The regional oceanic modeling system: a split-
573 explicit, free-surface, topography-following coordinate oceanic model. *Ocean Model* 9,
574 347–404. doi: 10.1016/j.ocemod.2004.08.002

575 Sun, D., T. Ito, & A. Bracco (2017) Oceanic uptake of oxygen during deep convection events
576 through diffusive and bubble mediated gas exchange *Global Biogeochem. Cycles*, 31,
577 https://doi.org/10/1002/2017GB005716

578 Travis L.D. (1978). Nature of atmospheric dynamics on Venus from power spectrum analysis of
579 Mariner 10 images. J. Atmos. Sci., 35, 1584-1595, doi: 10.1175/1520-
580 0469(1978)035<1584:NOTADO>2.0.CO;2

581 Zhong, Y., A. Bracco, J. Tian, J. Dong, W., Zhao, Z. Zhang (2017), Observed and simulated
582 vertical pump of an anticyclonic eddy in the South China Sea. Scientific Report , 44011,
583 doi:10.1038/srep44011

584 Zhong Y., and A. Bracco (2013), Submesoscale impacts on horizontal and vertical transport in the
585 Gulf of Mexico, *J. Geoph. Res. - Oceans*, 118, 5651-5668, doi:10.1002/jgrc.20402

586

Date	Orbit #	Orbit type	Pole	Average Resolution	Images #
02/02/2017	4	MWR	North	51 km	9
			South	55 km	11
05/19/2017	6	MWR	North	23 km	45
			South	59 km	12
09/01/2017	8	GRAV	South	47 km	18
10/24/2017	9	MWR	North	39 km	40
			South	16 km	40
12/16/2017	10	GRAV	North	15 km	14
02/07/2018	11	GRAV	South	44 km	17
05/24/2018	13	GRAV	South	53 km	12
07/16/2018	14	GRAV	South	57 km	10
09/07/2018	15	GRAV	South	61 km	23
12/21/2018	17	GRAV	South	49 km	16
02/12/2019	18	GRAV	South	46 km	14

Figure 1.

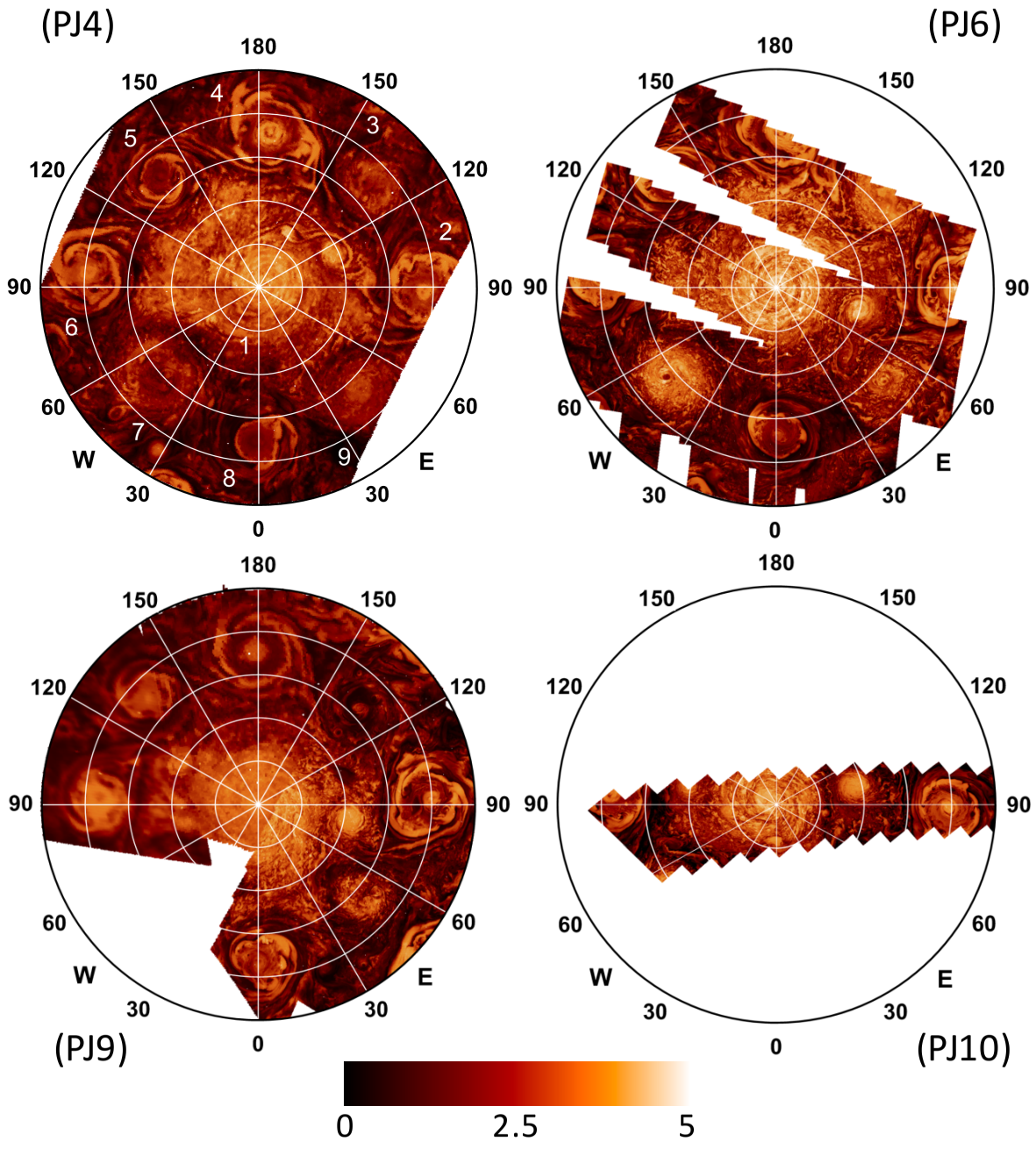
(PJ4)
(PJ6)
(PJ9)
(PJ10)
180
150
120
90
60
30
0
W
E
1
2
3
4
5
6
7
8
9
0
2.5
5

Figure 2.

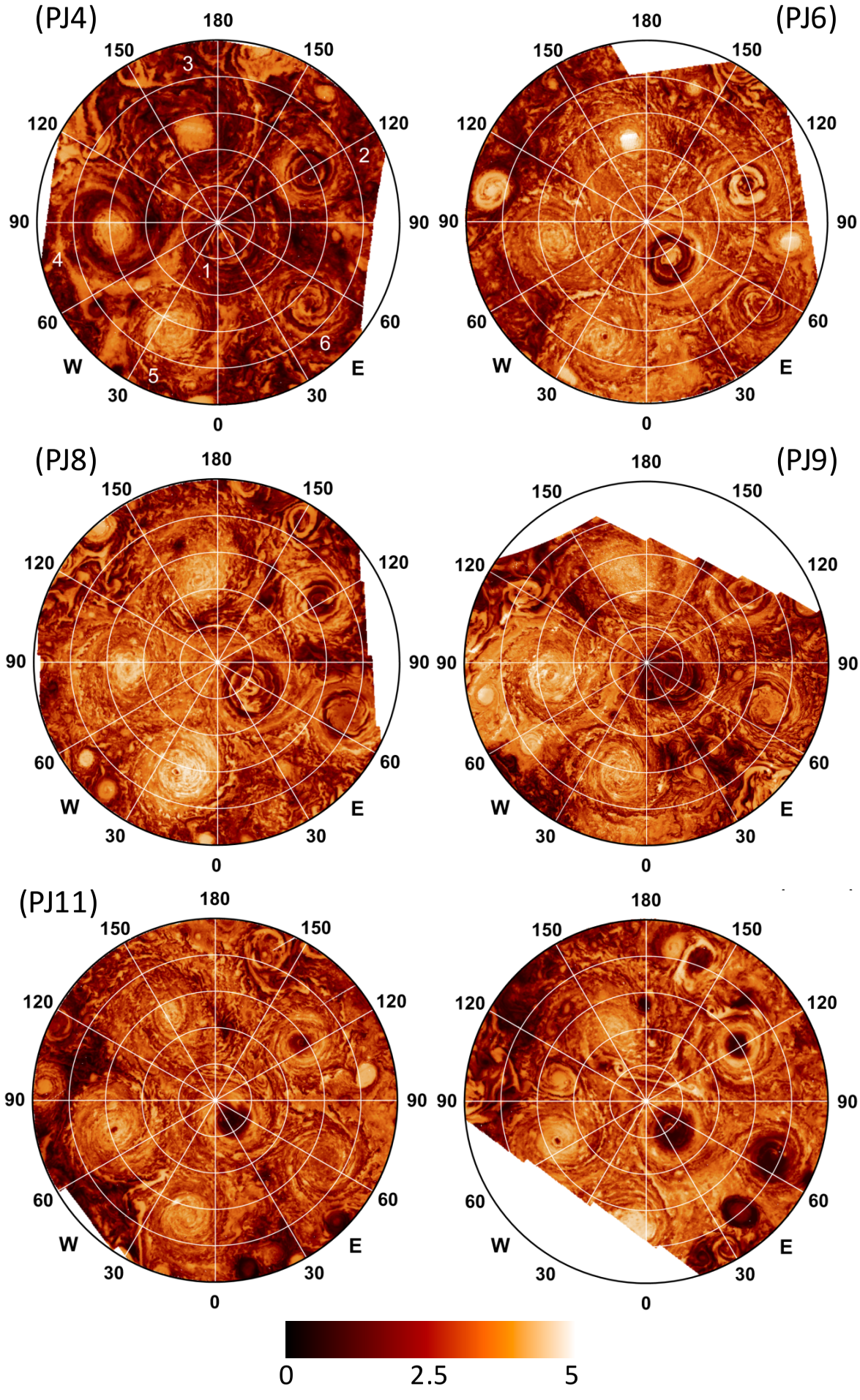
(PJ4)
(PJ6)
(PJ8)
(PJ9)
(PJ11)
180
150
120
90
60
30
0
W
E
1
2
3
4
5
6
0
2.5
5

Figure 3.

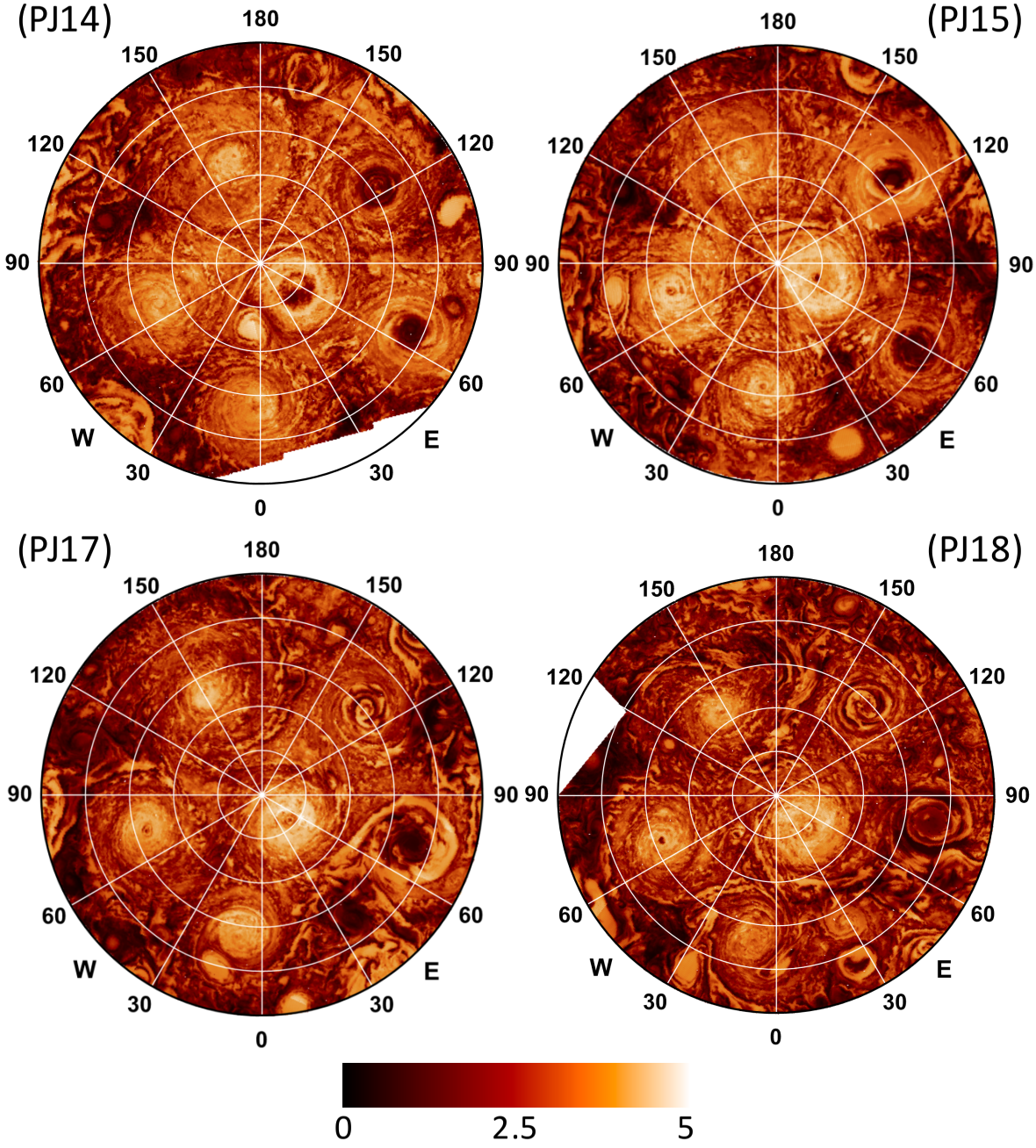
(PJ14)
(PJ15)
(PJ17)
(PJ18)
180
150
120
90
60
30
0
W
E
0
2.5
5

Figure 4.

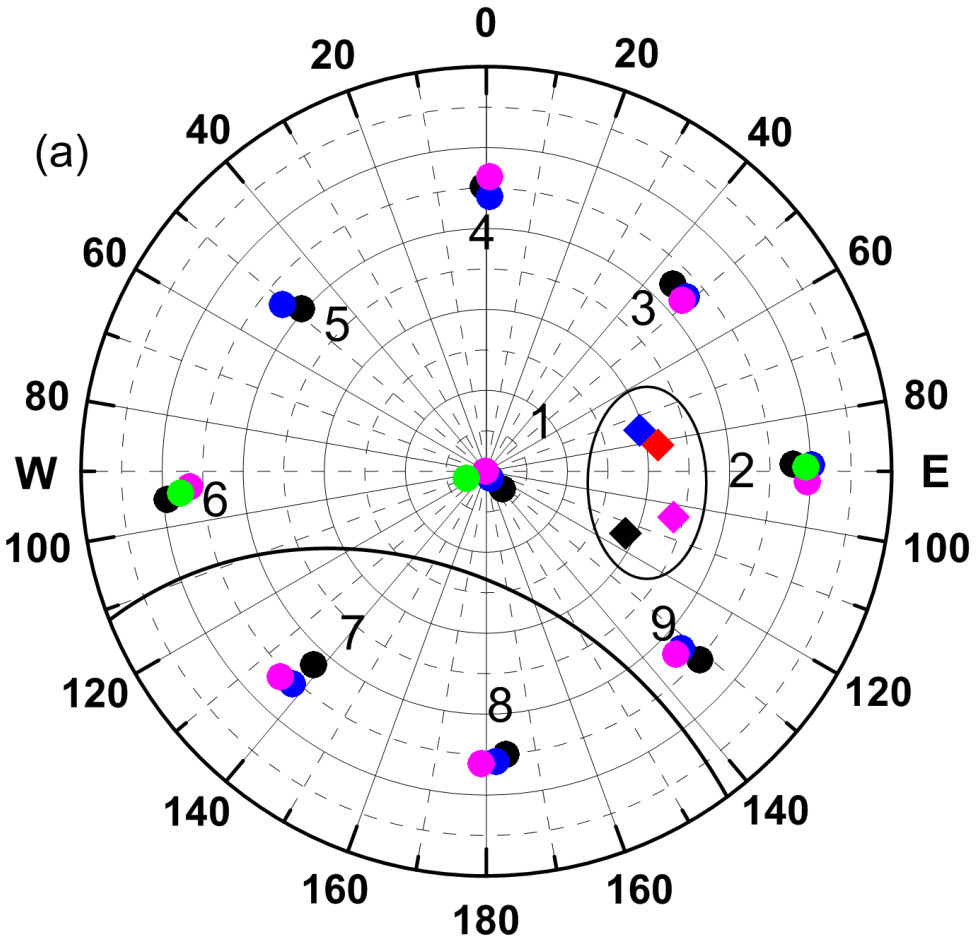
(a)
0
20
40
60
80
W
100
120
140
160
180
E
1
2
3
4
5
6
7
8
9
PJ04 PJ6 PJ9 PJ10

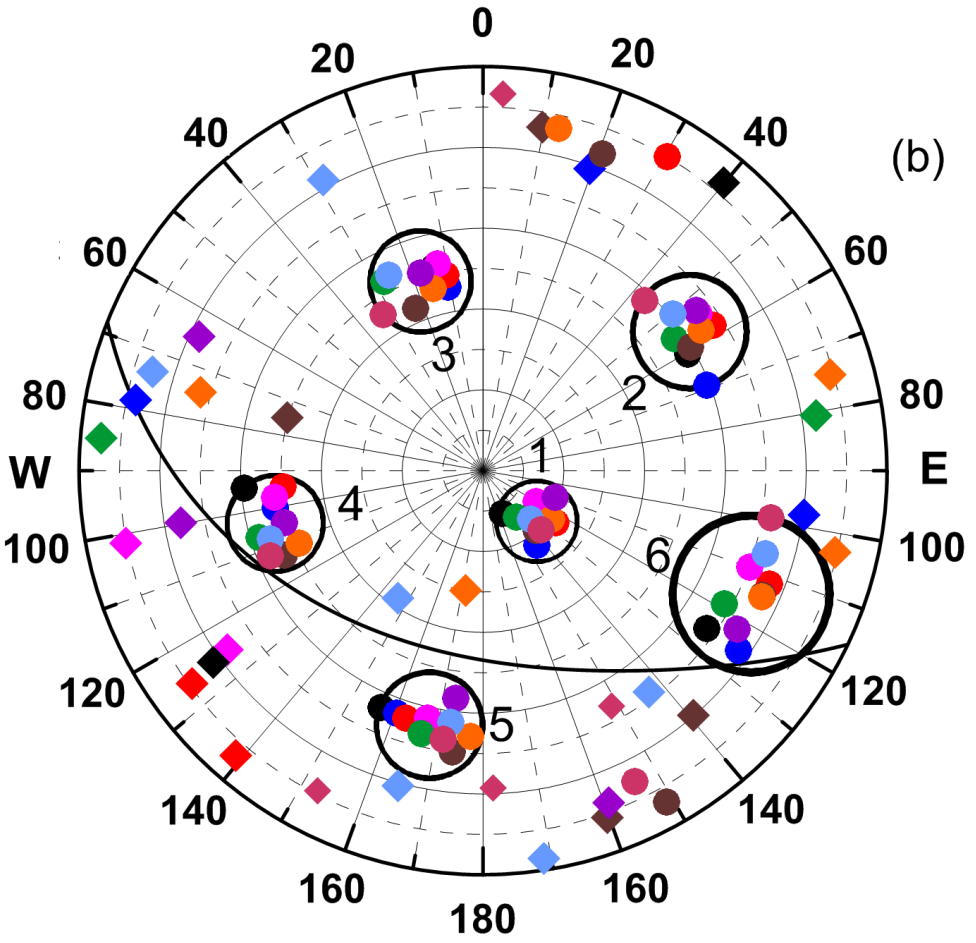
(b)
0
20
40
60
80
W
100
120
140
160
180
E
1
2
3
4
5
6
PJ04 PJ6 PJ8 PJ9 PJ11 PJ13 PJ14 PJ15 PJ17 PJ18

Figure 5.

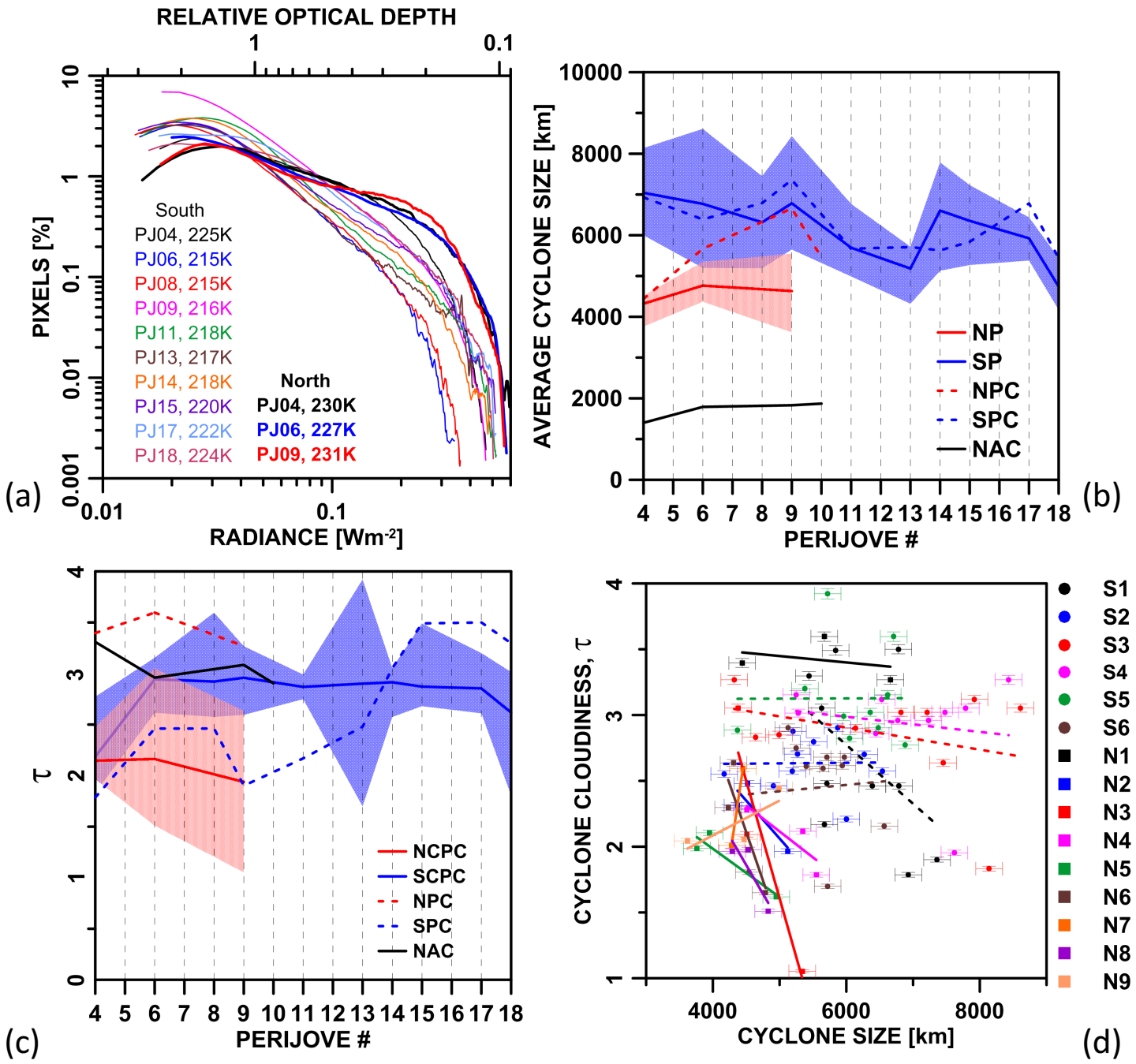
RELATIVE OPTICAL DEPTH
1
0.1
10
1
0.1
0.01
0.001
PIXELS [%]
South
PJ04, 225K
PJ06, 215K
PJ08, 215K
PJ09, 216K
PJ11, 218K
PJ13, 217K
PJ14, 218K
PJ15, 220K
PJ17, 222K
PJ18, 224K
North
PJ04, 230K
PJ06, 227K
PJ09, 231K
0.01
0.1
RADIANCE [Wm-2]
(a)
AVERAGE CYCLONE SIZE [km]
10000
8000
6000
4000
2000
0
NP
SP
NPC
SPC
NAC
4 5 6 7 8 9 10 11 12 13 14 15 16 17 18
PERIJOVE #
(b)
τ
4
3
2
1
0
NCPC
SCPC
NPC
SPC
NAC
4 5 6 7 8 9 10 11 12 13 14 15 16 17 18
PERIJOVE #
(c)
CYCLONE CLOUDINESS, τ
4
3
2
1
4000
6000
8000
CYCLONE SIZE [km]
S1
S2
S3
S4
S5
S6
N1
N2
N3
N4
N5
N6
N7
N8
N9
(d)

Figure 6.

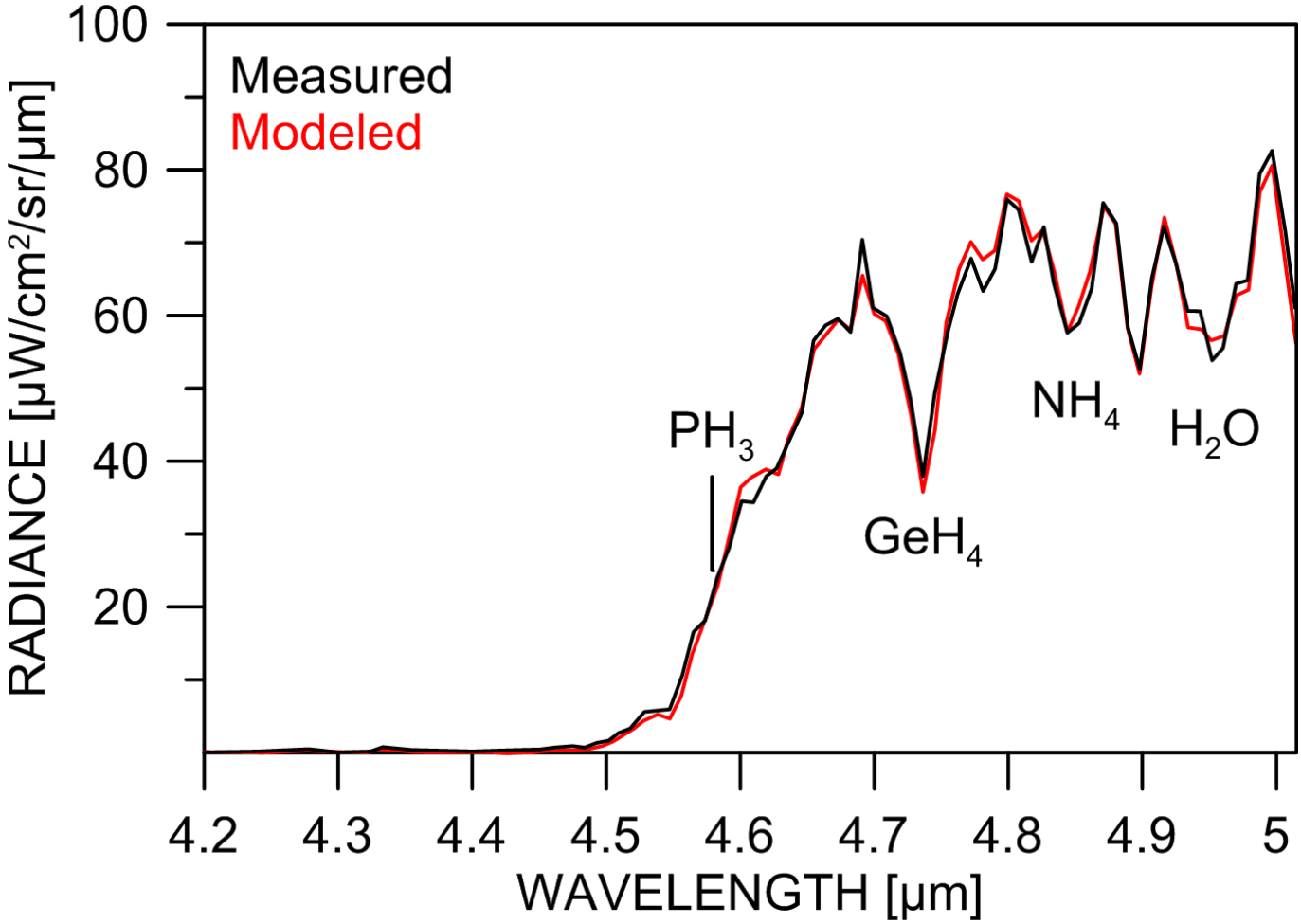
Measured
Modeled
RADIANCE [μW/cm²/sr/μm]
100
80
60
40
20
PH3
GeH4
NH4
H2O
4.2
4.3
4.4
4.5
4.6
4.7
4.8
4.9
5
WAVELENGTH [μm]

Figure 7.

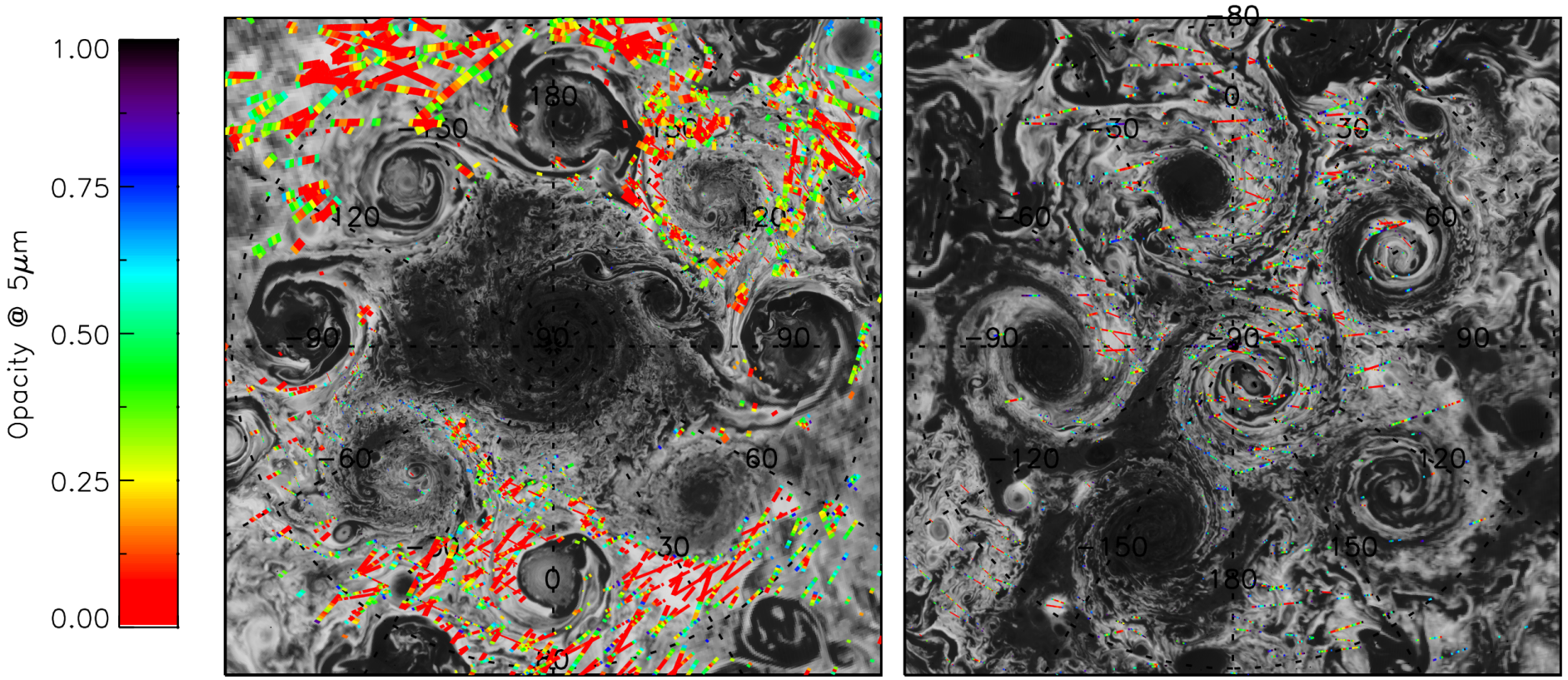
Opacity @ 5μm
1.00
0.75
0.50
0.25
0.00
180
−150
120
−120
−90
90
−60
60
−30
30
0
−80
−150
150
180

Figure 8.

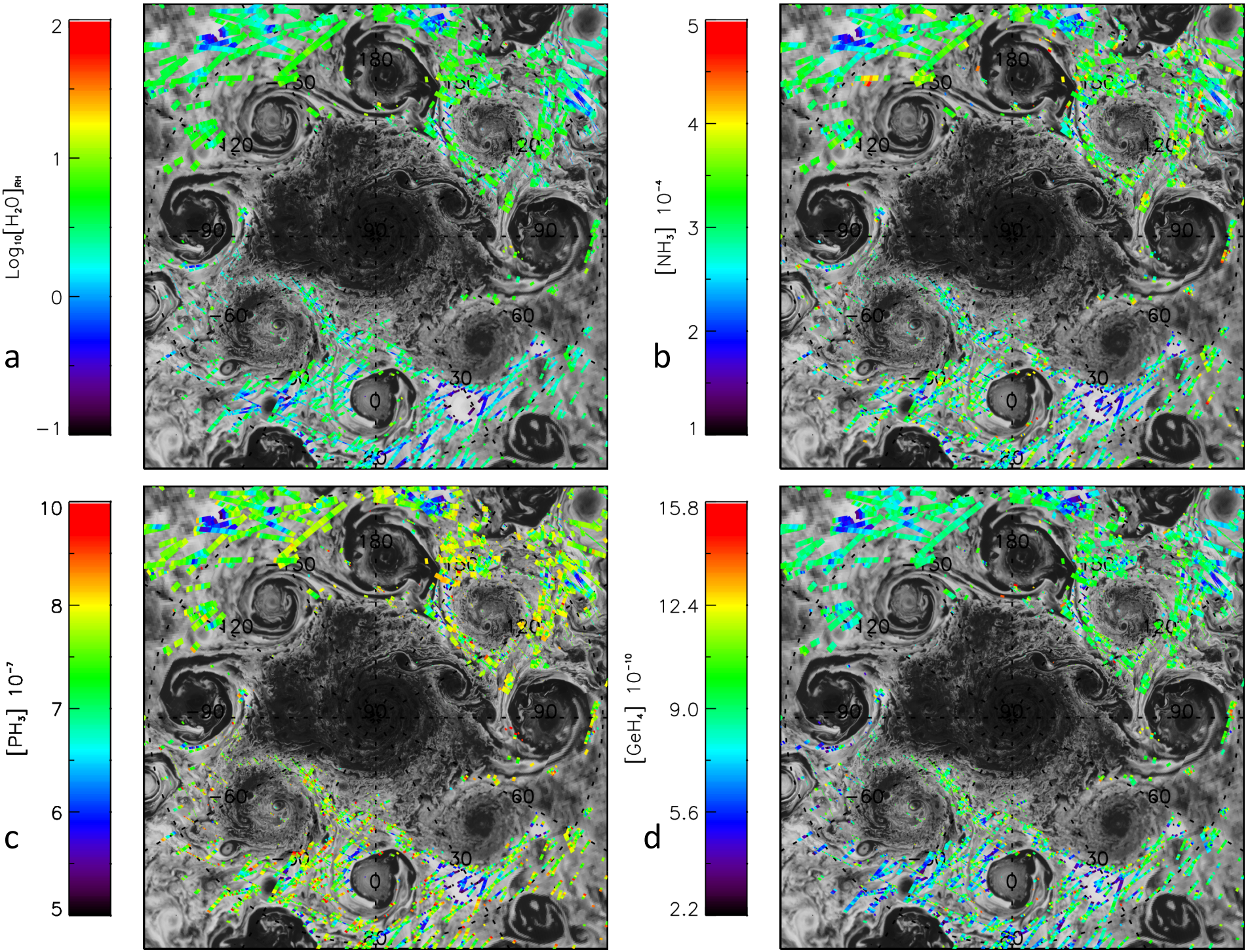
a
$\mathrm{Log_{10}[H_2O]_{RH}}$
2
1
0
−1
b
$[NH_3]\ 10^{-4}$
5
4
3
2
1
c
$[PH_3]\ 10^{-7}$
10
8
7
6
5
d
$[GeH_4]\ 10^{-10}$
15.8
12.4
9.0
5.6
2.2
180
−150
120
−120
90
−90
60
−60
30
−30
0

Figure 9.

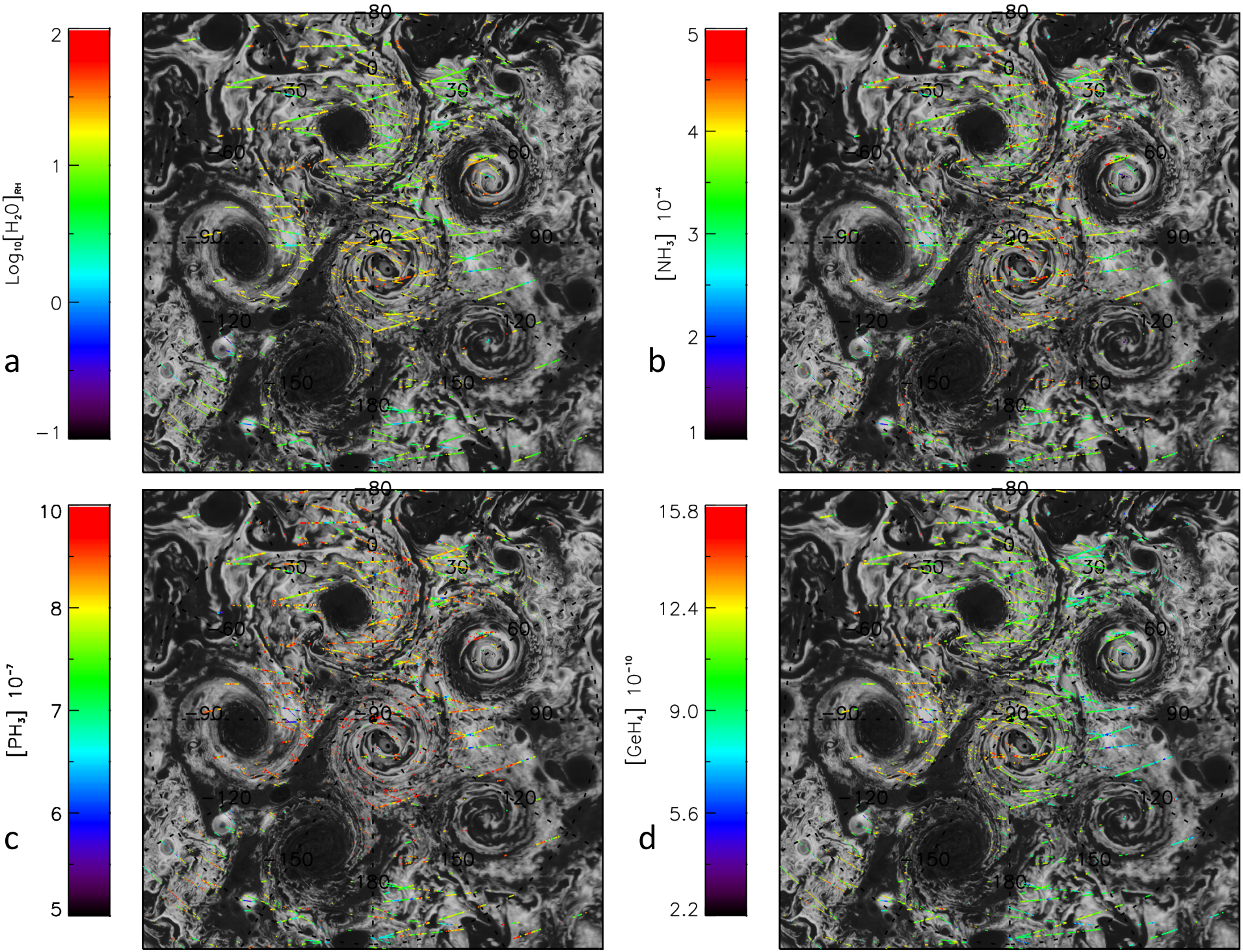
a
$\mathrm{Log_{10}[H_2O]_{RH}}$
2
1
0
−1
b
$[NH_3]\ 10^{-4}$
5
4
3
2
1
c
$[PH_3]\ 10^{-7}$
10
8
7
6
5
d
$[GeH_4]\ 10^{-10}$
15.8
12.4
9.0
5.6
2.2
−80
0
−30
30
−60
60
−90
90
−120
120
−150
150
180

Figure 10.

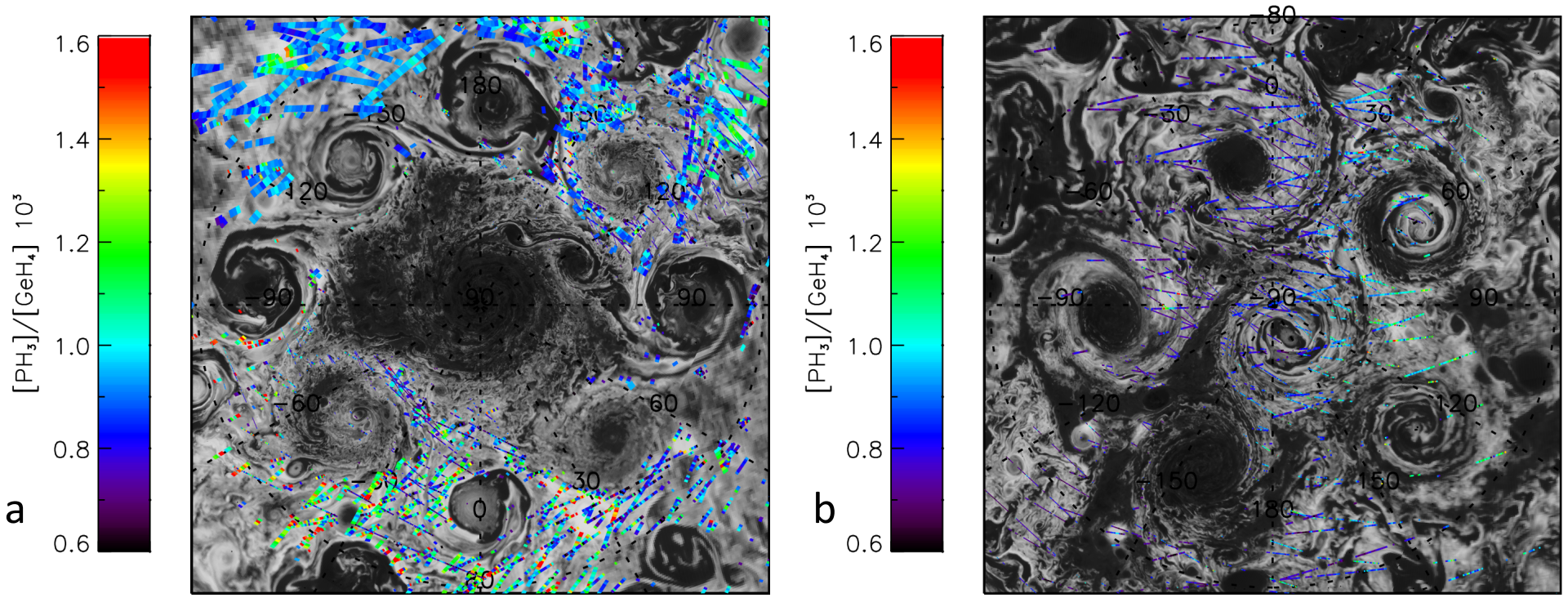
a
b
[PH3]/[GeH4] 10³
1.6
1.4
1.2
1.0
0.8
0.6
180
−150
150
−120
120
−90
90
−60
60
−30
30
0
−80

Figure 11.

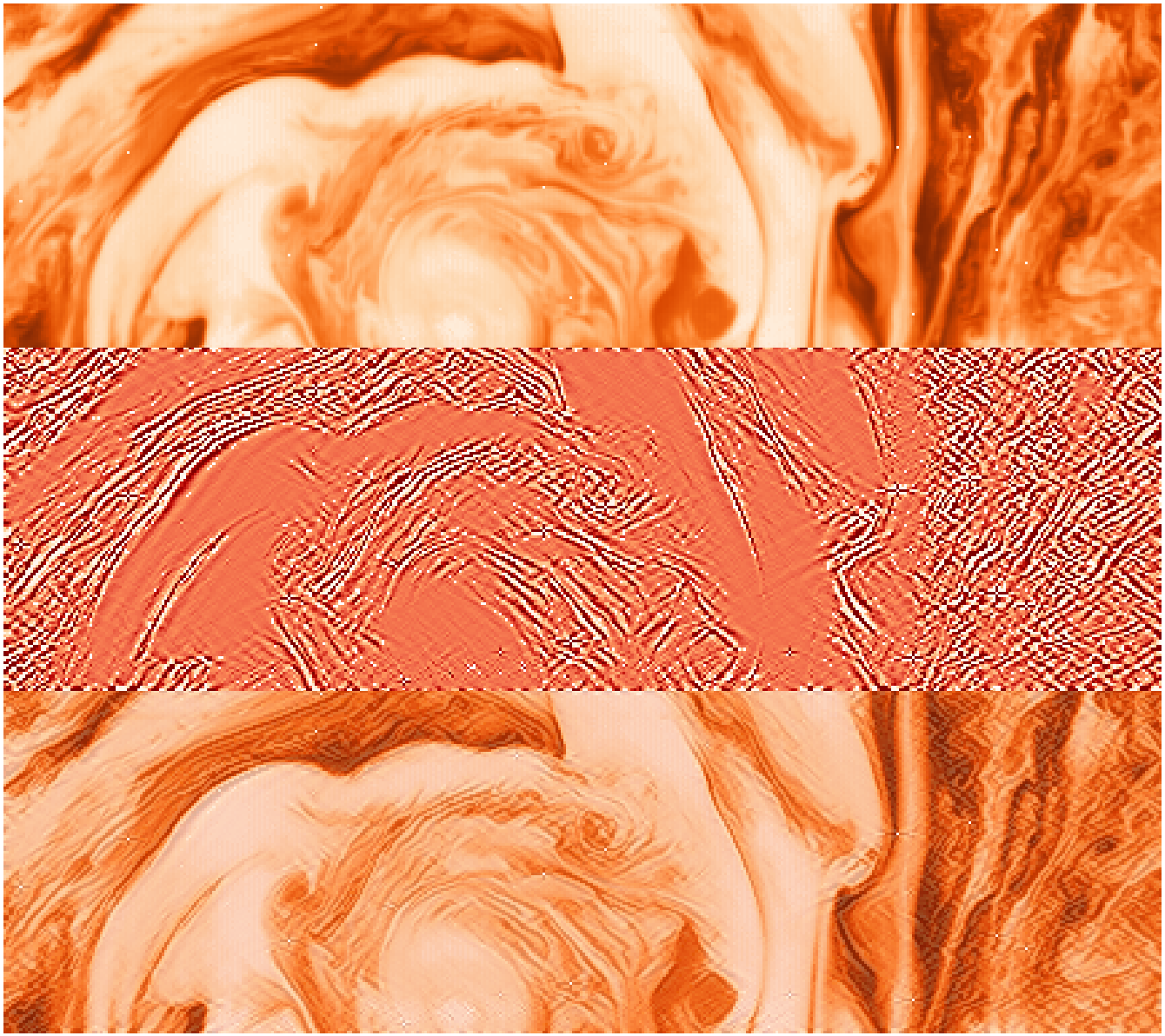

Figure 12.

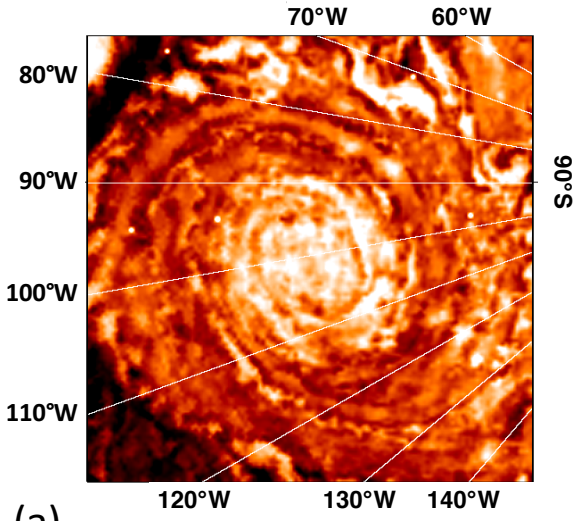
70°W
60°W
80°W
90°W
100°W
110°W
90°S
120°W
130°W
140°W

(a)

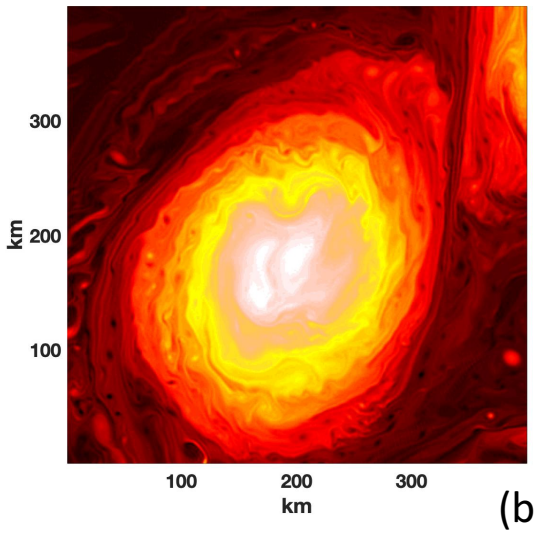
300
200
100
km
100
200
300
km

(b)

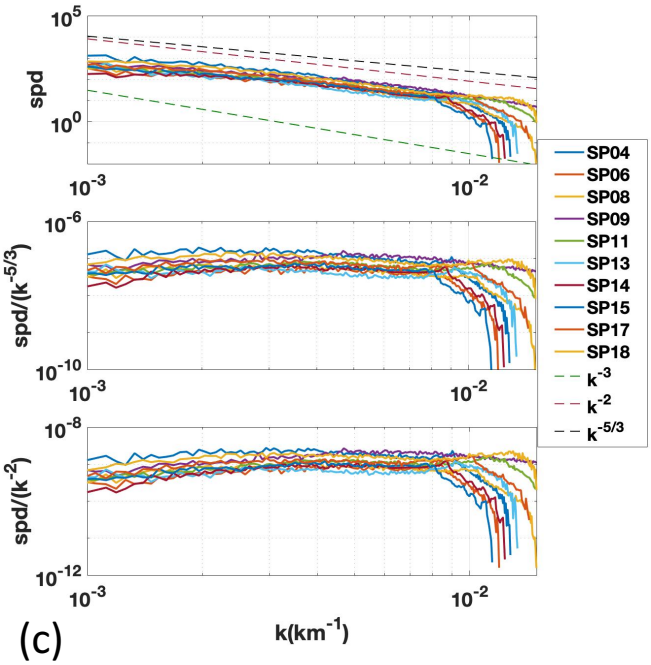
spd
spd/(k^-5/3)
spd/(k^-2)
k(km^-1)
SP04
SP06
SP08
SP09
SP11
SP13
SP14
SP15
SP17
SP18
k^-3
k^-2
k^-5/3

(c)

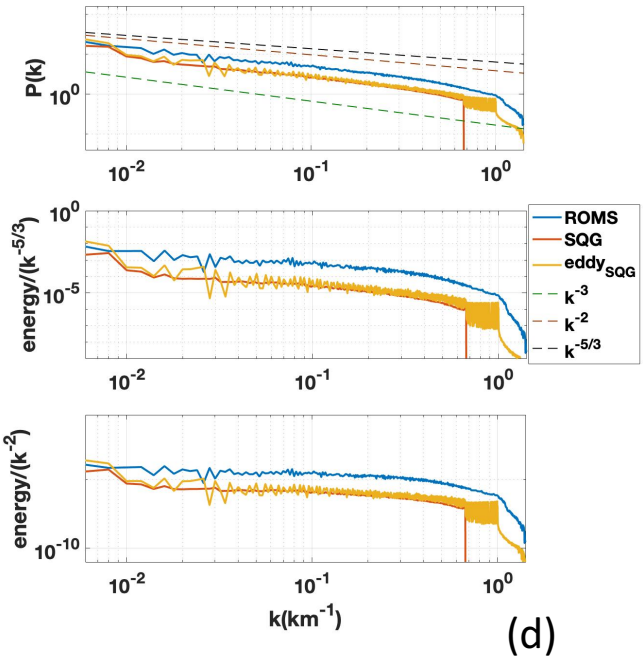
P(k)
energy/(k^-5/3)
energy/(k^-2)
k(km^-1)
ROMS
SQG
eddy_SQG
k^-3
k^-2
k^-5/3

(d)